

Metasurface-mediated quantum entanglement via bound states in the continuum

Hannah Riley^{1,2}, Emmanuel Lassalle^{2,*}, Diego Romero Abujetas^{3,4},
Adam Stokes⁵, Ramon Paniagua-Dominguez^{2,†} and Ahsan Nazir^{1,‡}

¹*Department of Physics and Astronomy, The University of Manchester,
Oxford Road, Manchester M13 9PL, United Kingdom*

²*Institute of Materials Research and Engineering (IMRE), Agency for Science,
Technology and Research (A*STAR), 2 Fusionopolis Way,
Innovis #08-03, Singapore 138634, Republic of Singapore*

³*Physics Department, Fribourg University, Chemin de Musée 3, 1700 Fribourg Switzerland*

⁴*Department of Mathematics, Universidad de Castilla-La Mancha,
Avenida Carlos III s/n, 45071 Toledo, Spain and*

⁵*School of Mathematics, Statistics, and Physics, Newcastle University,
Newcastle upon Tyne NE1 7RU, United Kingdom*

Scalable quantum technologies demand entanglement between many distant quantum emitters (QEs), for which we propose using high- Q , spatially extended bound states in the continuum (BICs) in all-dielectric metasurfaces. We show that QE-BIC coupling efficiencies (β -factors) can exceed 80%, comparable to waveguides even without further mode engineering, but within a 2D geometry that naturally accommodates large QE arrays and relaxes strict emitter placement. Inter-QE entanglement is generated faster than in free space, is significantly amplified, and persists over several resonant wavelengths. Optimality requires large β -factors but moderately small Purcell factors. Our results establish all-dielectric metasurfaces as a practical, scalable platform for leading-edge quantum photonics.

I. INTRODUCTION

Achieving robust, scalable entanglement between quantum emitters (QEs) is central to the development of commercial quantum technologies. While perfect isolation would preserve entanglement indefinitely, practical systems inevitably suffer decoherence due to environmental interactions. To mitigate this, structured photonic environments are tailored to enhance QE interactions, supporting collective quantum effects [1–6]. One-dimensional (1D) waveguides, for example, have enabled long-range QE-QE coupling [7–10], with the most recent experimental example demonstrating enhanced coupling of quantum dots via a photonic crystal waveguide [11]. However, the intrinsic 1D geometry of waveguides poses a significant scalability challenge that could be overcome using two-dimensional (2D) architectures to generate entanglement across planar QE arrays.

Metasurfaces are planar arrays of engineered nanoparticles (“meta-atoms”) enabling sub-wavelength control of light that extends into the quantum regime [12, 13], while further offering scalability, fabrication, and integration advantages [14–18]. Jha et al. [19] demonstrated the potential of metasurfaces to effectively facilitate entanglement generation by considering atomic qubits in the metasurface far-field, but this setup requires precise free-atom positioning. More recently, Zundel et al. [20] have studied long-range interactions between QEs mediated by

lattice resonances in the near-field of a metallic metasurface. While this architecture enables compact integration with QE arrays, it introduces additional losses inherent to metallic systems.

Here, we propose harnessing the *bound states in the continuum* (BICs) of *all-dielectric* metasurfaces. BICs are localized wave states embedded within the radiation continuum but decoupled from it, preventing energy leakage [21–23]. First theorized by von Neumann and Wigner in 1929 [24] and named by Fonda in 1960 [25], ideal BICs exhibit infinite lifetime and quality factor (Q). In practice, imperfectly fabricated finite surfaces possess only quasi-BICs with very high but finite Q . Although inaccessible via far-field excitation, BICs can be efficiently excited by localized near-field sources [26–28].

We begin by introducing the composite system, within which the QEs are described using a Lindblad master equation. The metasurface-modified single and collective decay rates therein are directly related to local and cross densities of states (LDOS and CDOS) [29]. These quantities are computed for two distinct BICs, electric dipole (ED-BIC) and magnetic dipole (MD-BIC), which exhibit different maximum near-field coupling conditions. A combined analytic and numerical analysis yields β -factors that quantify emitter-BIC coupling [30–32] and determine the resulting dynamics. We use the concurrence to quantify QE-QE entanglement generated through spontaneous emission [33], and find an approximate expression in terms of β and Purcell factors.

We find that metasurfaces supporting BICs can mediate long-range interactions and entanglement between QEs over separations exceeding several resonant wavelengths, persisting indefinitely in the ideal case of an infinite metasurface. QE-BIC coupling efficiencies (β -

*Electronic address: emmanuel.lassalle@imre.a-star.edu.sg

†Electronic address: ramon.paniagua@imre.a-star.edu.sg

‡Electronic address: ahsan.nazir@manchester.ac.uk

factors) above 80% are achieved, exceptionally high for a 2D platform, and could be further improved through mode engineering and optimisation of the metasurface geometry. The resulting QE-QE entanglement depends almost exclusively on the β -factor, increasing monotonically with it. The metasurface also produces a notable Purcell effect that significantly accelerates entanglement generation, a key advantage for fast quantum gate operations.

II. RESULTS

A. System

We consider a pair of two-level quantum emitters $\mu = 1, 2$ (Fig. 1a), with ground and excited states $|g_\mu\rangle$ and $|e_\mu\rangle$ respectively, and with the same two-level transition energy $\hbar\omega_0$ where \hbar is the reduced Planck constant. The corresponding transition wavelength is $\lambda_0 = 2\pi c/\omega_0$ where c is the speed of light. We assume identical transition dipole moment magnitudes, $p_1 = p_2 = p$, but allow different orientations; $\hat{\mathbf{p}}_1 \neq \hat{\mathbf{p}}_2$ in general.

We consider the metasurface depicted in Fig. 1a, namely, a square array in the xy -plane with lattice constant $a = 400\text{nm}$, comprised of 21×21 silicon nanospheres each with radius $R = 100\text{nm}$ and refractive index $n = 3.5$ [34]. The QEs are placed at a vertical height $h = z - R = 4\text{nm}$ above the metasurface, enabling efficient near-field coupling to optical resonances. At this height, the dipoles can be considered weakly-coupled to the metasurface provided p does not exceed the value of roughly 90 Debye (see Supp. Info. Section A).

In this regime, the reduced density matrix $\rho(t)$ of the two-QE system satisfies a Lindblad master equation of the same form as that for free space dipoles, see for example Ref. [35]. Details are provided in Supp. Info. Section B. The master equation coefficients differ from those for free space and thereby account for the metasurface. They are expressible in terms of the dyadic Green's tensor for the Maxwell equations, \mathbf{G} , evaluated at the QE positions \mathbf{R}_μ and \mathbf{R}_ν , as

$$\Gamma_{\mu\nu} = \frac{2p_i p_j \omega_0^2}{\hbar \varepsilon_0 c^2} \Im(G_{ij}(\mathbf{R}_\mu, \mathbf{R}_\nu, \omega_0)), \quad (1)$$

and

$$\Omega_{\mu \neq \nu} = -\frac{\omega_0^2}{\hbar \varepsilon_0 c^2} p_i p_j \Re(G_{ij}(\mathbf{R}_\mu, \mathbf{R}_\nu, \omega_0)). \quad (2)$$

where ε_0 is the vacuum permittivity. We assume the Einstein summation convention for repeated Cartesian indices i and j .

The two-QE system comprises four (Dicke) levels and two decay channels with rates $\Gamma_{11} \pm \Gamma_{12}$ (Fig. 1b). We refer to Γ_{11} (resp. Γ_{22}), Γ_{12} , and Ω_{12} as the *single emitter decay rate* of QE 1 (resp. QE 2), the *collective decay rate* and the *collective coupling rate*, respectively. The terms

$\Gamma_{\mu\mu}$ and Γ_{12} when normalized by the free space decay rate of a single dipole $\Gamma_0 = \omega_0^3 p^2 / (3\pi \varepsilon_0 \hbar c^3)$, only depend on characteristics of the electromagnetic environment, being related to the LDOS and CDOS respectively, which are in turn proportional to the imaginary part of \mathbf{G} [29].

In free space, significant dipole-dipole interactions only occur for QE separations d satisfying $d < \lambda_0$ [36]. Due to the 4π solid angle radiance of the dipoles, only a small quantity of radiation from the source dipole is emitted in the direction of the target dipole. We will show that QE-metasurface platforms can be engineered to enhance desired dipole emission through coupling to resonant modes, facilitating dipole-dipole interactions over macroscopic separations $d > \lambda_0$. We consider two types of optical resonance, namely, the electric dipole BIC and the magnetic dipole BIC [34]. The LDOS and the CDOS are computed numerically using the Python package SMUTHI [37] (see Methods).

B. Metasurface local density of states (LDOS)

Figs. 2(a) and (b) show the LDOS Γ_{11}/Γ_0 as a function of λ_0 in the vicinity of the resonance wavelengths of the ED-BIC and MD-BIC, respectively. The maximum value is called the Purcell factor F_p , which is shown in Figs. 2(c) (ED-BIC) and (d) (MD-BIC), as a function of vertical height above the metasurface. For the ED-BIC, $F_p = 46.9$ occurring at resonance wavelength $\lambda_0 = 552\text{nm}$, and for the MD-BIC, $F_p = 13.7$ occurring at $\lambda_0 = 708.9\text{nm}$. Although it possesses a smaller Purcell factor, the MD-BIC has a much narrower linewidth [smaller full width at half maximum (FWHM)], implying a larger Q -factor, which becomes relevant in the strong-coupling regime (see Supp. Info. Section A).

The orientation and lateral position of the emitters are chosen to maximise the coupling. In the case of the ED-BIC, the emitter must be centred on a nanosphere with out-of-plane orientation (z -direction). The MD-BIC offers greater flexibility; the emitter can be located anywhere on the circle of radius $r = 0.163a$ centered on a nanosphere, with in-plane orientation tangential to this circle. Lateral spatial dependence at fixed orientations of ED- and MD-BIC coupling is shown in the insets of Figs. 2(c) and (d), respectively.

For both BICs the decay with vertical position z of the QE-BIC coupling (Purcell factor) is essentially exponential, admitting a close fit to the function $1 + Ae^{-B(z-R)/a}$, where A and B are dimensionless fitting parameters [grey dashed lines Figs. 2(c) and (d)]. This behaviour is characteristic of near-field coupling to a mode bound to the surface, and implies that varying z enables predictable control of the coupling strength.

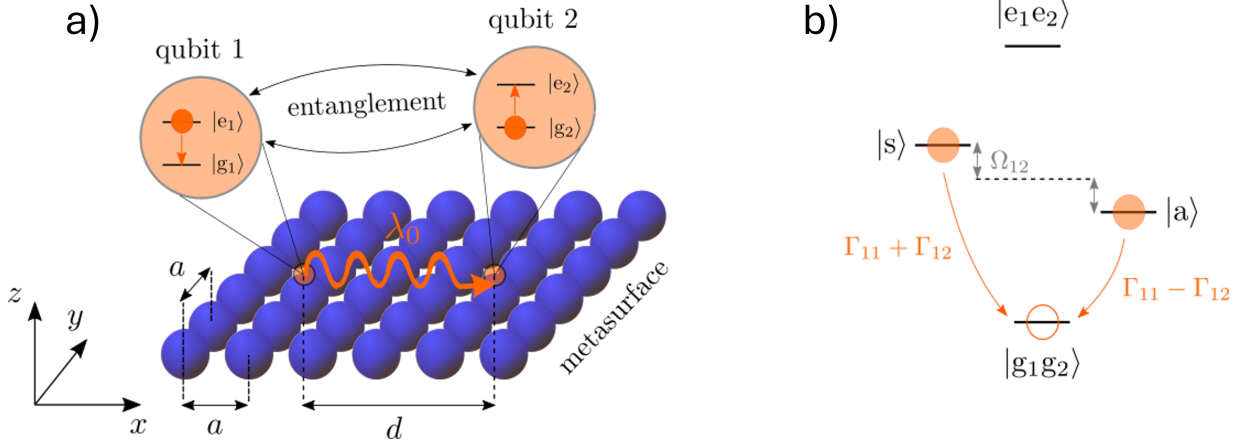


FIG. 1: Long-range metasurface-mediated interactions between two qubits. (a) Initially uncorrelated QEs (qubits) spontaneously emit into delocalized BIC modes, resulting in entanglement over distances much larger than the wavelength of emitted photons. (b) Dicke states of the two emitter system are connected by decay channels with rates $\Gamma_{11} \pm \Gamma_{12}$.

C. Metasurface cross density of states (CDOS)

We now consider the coupling between two QEs, as quantified by the CDOS Γ_{12}/Γ_0 . Fig. 3 shows the lateral spatial dependence of the CDOS when QE1 is fixed while QE2 is scanned across the surface. The position and orientation of QE1 are chosen to maximise the coupling to the BIC, as in Figs. 2(a) and (b). In the case of the ED-BIC, the orientation of QE2 matches that of QE1, while for the MD-BIC, we consider two in-plane orientations of QE2, as parallel and orthogonal to that of QE1.

There is a significant enhancement of the CDOS when the second QE is located above the nanospheres of the metasurface, but this is different in each of the three cases considered. For the MD-BIC, the CDOS associated with any in-plane orientation can be generated by summing the heatmaps Fig. 3(b) and Fig. 3(c) after they have been weighted by the magnitude of the dipole moment in the x and y directions, respectively.

Unlike the LDOS, the CDOS can take negative values, but the inequality $|\Gamma_{12}| \leq \sqrt{\Gamma_{11}}\sqrt{\Gamma_{22}}$, which results from the properties of the Green's tensor, is always satisfied [29]. Coupling to the BIC modes provides a large CDOS over separations that exceed several wavelengths. For comparison, we plot in Supp. Info. Section C the free space CDOS, which is only non-negligible for near-field lateral separations $d < \lambda_0$. Figs. 4(a) and (b) show cuts of the CDOS for the ED-BIC and MD-BIC along the white dashed lines in Figs. 3 (a) and (c), respectively. As the separation increases, periodic oscillations are observed, with gradual decays that, however, are different in the ED- and MD-BIC cases. The decay is primarily a finite-size effect, as can be deduced by comparison with the infinite surface case (see next section).

D. BIC β -factors

When considering an infinite metasurface, closed expressions can be obtained for collective decay rates Γ_{12} , because the CDOS is expressible in terms of an integral over the first Brillouin zone (see Supp. Info. Section D). Assuming a single-mode approximation of the metasurface, we obtain a product of oscillatory and envelope functions in the form

$$\Gamma_{12}(d) = \underbrace{\Gamma_{11}\beta}_{\text{env}(d)} \underbrace{J_0(k_{\parallel}^{\text{res}}|d|) \sum_{n=0}^N c_n \cos\left(2n\pi \frac{d}{a}\right)}_{\text{osc}(d)}, \quad (3)$$

where Γ_{11} denotes the maximum decay rate of QE1, while $\beta \in [0, 1]$ is the so-called β -factor, defined as the ratio of the emission rate into the BIC mode and Γ_{11} [30–32]. The oscillatory part $\text{osc}(d)$ is an $(N + 1)$ -term Fourier cosine series. For the ED-BIC $N = 4$ with

$$c_0 = 0.273, \quad c_1 = 0.516, \quad c_2 = 0.160, \\ c_3 = 0.048, \quad c_4 = 0.001,$$

while for the MD-BIC $N = 2$ with

$$c_0 = 0.642, \quad c_1 = 0.351, \quad c_2 = 0.005.$$

Within $\text{env}(d) = J_0(k_{\parallel}^{\text{res}}d)$, J_0 denotes the Bessel function of the first kind while the parameter $k_{\parallel}^{\text{res}}$ characterizes the detuning between ω_0 and the BIC resonance, and vanishes for a perfect frequency match, yielding $\text{env}(d) = 1$. Numerical results for the infinite metasurface case are obtained using a coupled electric and magnetic dipole (CEMD) code developed in Refs. [34, 38] (see Methods), because SMUTHI is not applicable.

The parameters β and $k_{\parallel}^{\text{res}}$ are obtained by fitting Eq. (3) to the numerical results. This yields $k_{\parallel}^{\text{res}} =$

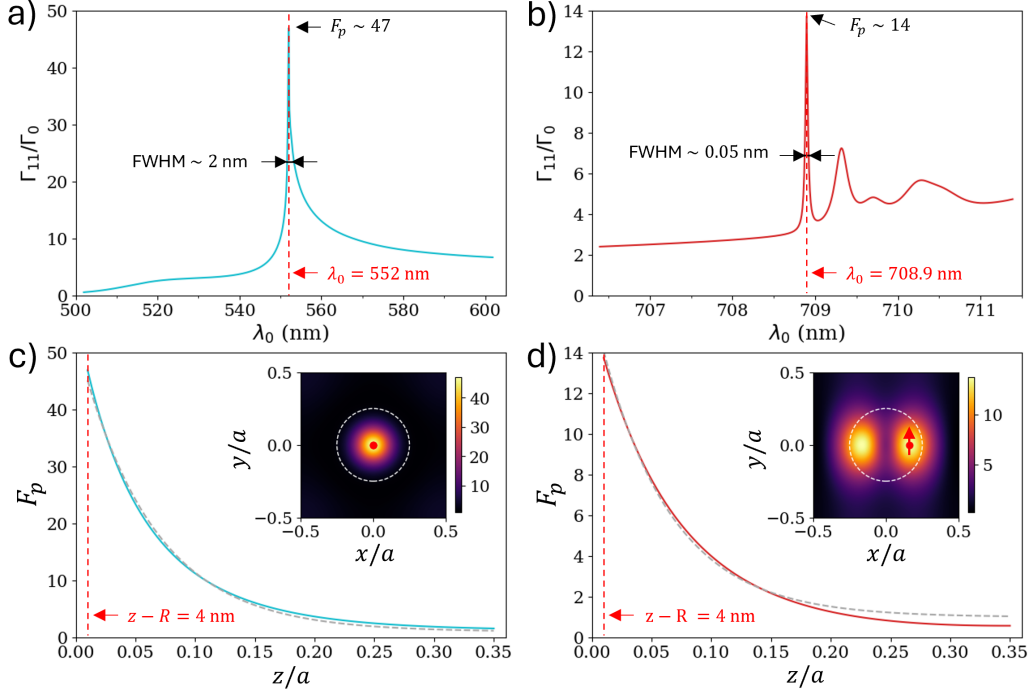


FIG. 2: LDOS Γ_{11}/Γ_0 as a function of λ_0 with $h = 4$ nm for the ED-BIC (a) and MD-BIC (b), and the Purcell factor F_p as a function of height above the metasurface for the ED-BIC (c) and MD-BIC (d). In (a) and (b) dashed red lines show BIC resonance wavelengths, and the emitter's position and orientation are chosen to maximise the coupling. In (c) and (d) dashed red lines occur at height $h = z - R = 4$ nm. Dashed grey lines are exponential fits of the form $1 + Ae^{-B(z-R)/a}$ with fitting parameters $A = 51.80$ and $B = 16.05$ (c), and $A = 15.47$ and $B = 16.97$ (d). In (a) and (c) the emitter is located at the central nanosphere ($x = 0, y = 0$) and possesses out-of-plane orientation along the z -axis. In (b) and (d) the emitter's lateral position is slightly off-centre from the central nanosphere, located at $(x = 0.163a, y = 0)$, with in-plane orientation along the y -axis. The peak LDOS is the Purcell factor. In (a) $F_p = 46.9$ at $\lambda_{\text{BIC}} = 552.0$ nm, and in (b) $F_p = 13.7$ at $\lambda_{\text{BIC}} = 708.9$ nm. Insets for (c) and (d): Purcell factor as a function of lateral position in the plane at $z = R + h$ for an emitter with out-of-plane orientation along the z -axis (c) and in-plane orientation along the y -axis (d). Red dots show the positions of maximum coupling considered in (a) and (b). Red arrows show the orientation of the emitter dipole moments. Dashed white circles show a nanosphere cross-section.

$0.219 \text{ rad}/\mu\text{m}$ and $\beta = 75.18\%$ for the ED-BIC, and $k_{\parallel}^{\text{res}} = 0.125 \text{ rad}/\mu\text{m}$ and $\beta = 82.43\%$ for the MD-BIC. Figs. 4(c) and (d) show both the numerical results and fits to these of Eq. (3). Both β -factors are remarkably high; close to those calculated for photonic crystal waveguides (PCWs) [30, 31]. Importantly, however, BIC modes are delocalized in 2D, making metasurface platforms much more readily integrable with large ensembles of QEs in 2D arrays. Moreover, while for comparison with existing literature we have chosen metasurface parameters identical to those in Ref. [34], optimisation of the metasurface geometry and meta-atom type (nanodisks, -rings etc.) could significantly increase β values.

A real (finite) metasurface possesses a broader BIC resonance resulting in an effective detuning from ω_0 , but this can be accounted for within Eq. (3) via $k_{\parallel}^{\text{res}}$, again treated as a fitting parameter. Figs. 4(a)-(b) show numerical re-

sults and fits to these of Eq. (3), for the finite metasurface consisting of 21×21 nanoparticles [Figs. 4(a)-(b)]. The fitting yields $k_{\parallel}^{\text{res}} = 0.581 \text{ rad}/\mu\text{m}$ and $\beta = 44.80\%$ for the ED-BIC, and $k_{\parallel}^{\text{res}} = 0.562 \text{ rad}/\mu\text{m}$ and $\beta = 81.79\%$ for the MD-BIC.

Agreement between numerical results and Eq. (3) is good for both the infinite and the finite metasurface, and for both BIC types, though it is slightly better for the ED-BIC. This may be because non-resonant modes excluded in the single-mode treatment that yields Eq. (3), are more important in the case of the MD-BIC, as seen by comparing Figs. 2 (a) and (b). Similarly, while agreement is excellent at large distances for which the interaction is mediated almost completely by the BIC mode, as d is reduced, non-resonant modes play an increasingly important role, so the single-mode approximation becomes poorer. The critical distances below which deviation be-

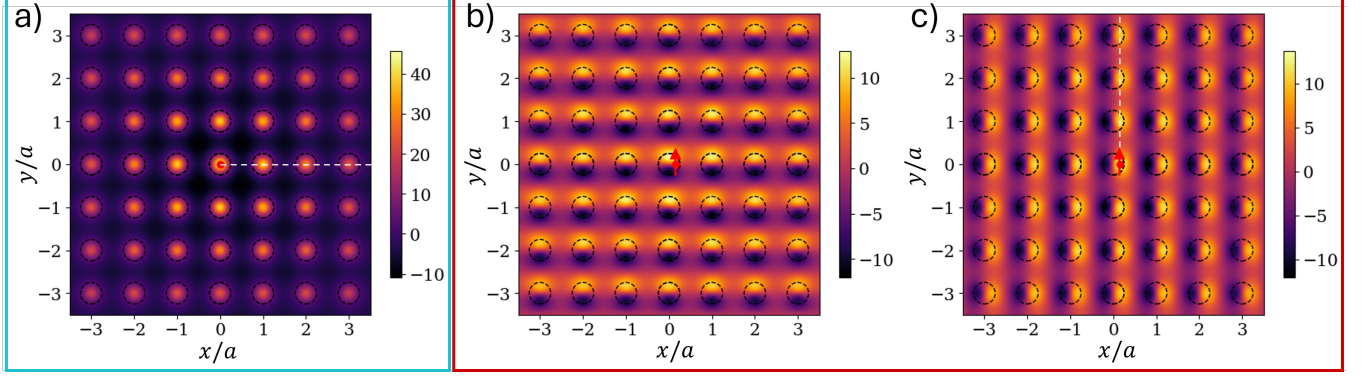


FIG. 3: Lateral spatial dependence of the CDOS Γ_{12}/Γ_0 of two emitters at height $h = z - R = 4$ nm above the metasurface, shown for an area of 7×7 nanospheres centered on the central nanosphere, for: (a) The ED-BIC at resonance wavelength $\lambda_{\text{BIC}} = 552.0$ nm with QE1 at $(x = 0, y = 0)$ and with out-of-plane orientation (red dot, inset Fig. 2c), while QE2 is laterally scanned across the metasurface with the same out-of-plane orientation. (b) and (c) The MD-BIC at resonance wavelength $\lambda_{\text{BIC}} = 708.9$ nm with QE1 at $(x = 0.163a, y = 0)$, and with in-plane orientation along the y -axis (red dot/arrow, inset of Fig. 2d), while QE2 is laterally scanned across the metasurface with (b) in-plane orientation along the x -axis, *orthogonal* to the orientation of QE1, and (c) in-plane orientation along the y -axis, *parallel* to the orientation of QE1. The dashed white lines show a cut along x at $y = 0$ (a), and a cut along y at $x = 0.163a$ (c). Dashed black circles show nanosphere cross-sections.

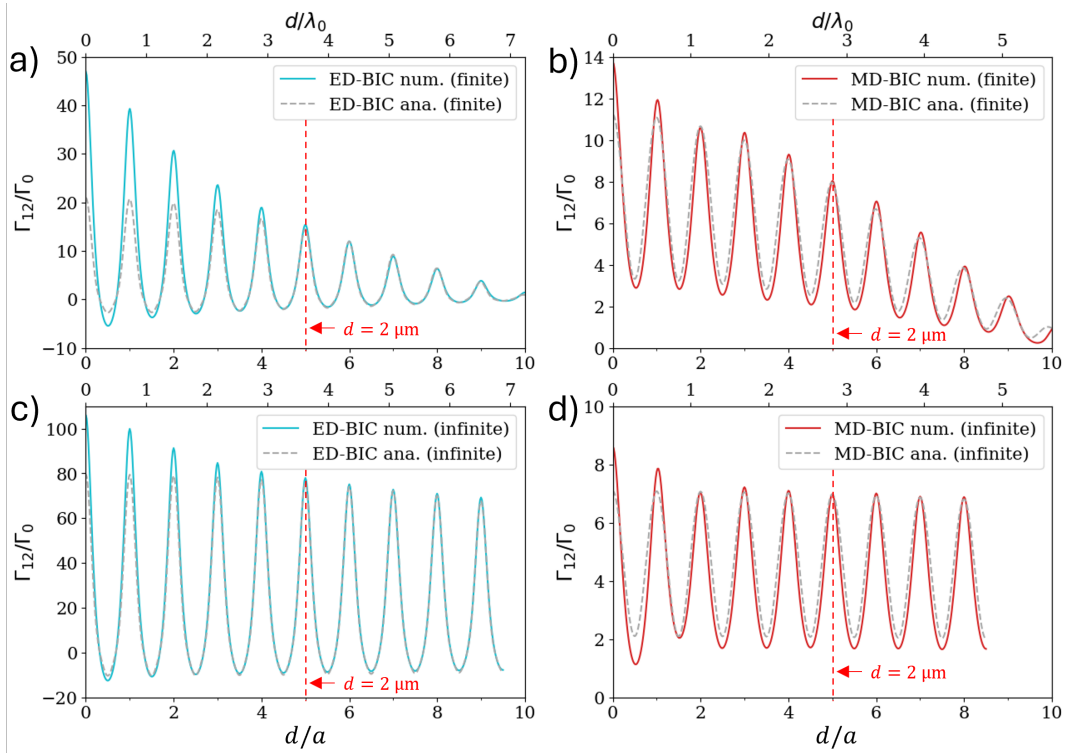


FIG. 4: The CDOS Γ_{12}/Γ_0 is plotted as a function of d for (a) the ED-BIC along $y = 0$ [white dashed line Fig. 3(a)], and (b) the MD-BIC along $x = 0.163a$ [white dashed line Fig. 3(c)]. The dashed grey curves in (a) and (b) are fits to Eq. (3) with fitting parameters: $\beta = 44.80\%$ and $k_p = 0.581$ rad/ μm for the ED-BIC and $\beta = 81.79\%$ and $k_p = 0.562$ rad/ μm for the MD-BIC. (c) and (d): Same as (a) and (b) for the *infinite* metasurface. Fitting parameters: $\beta = 75.18\%$ and $k_p = 0.219$ rad/ μm for the ED-BIC and $\beta = 82.43\%$ and $k_p = 0.125$ rad/ μm for the MD-BIC. The fits are made over the range $d \geq 5a$ ($d \geq 2a$) for the ED- (MD-)BIC, for which Γ_{12} is well-approximated by Eq. (3).

comes most significant are approximately $d = 5a$ and $d = 2a$ for the ED- and MD-BICs, respectively (see Supp. Info. Section E).

The finite size of a real metasurface significantly reduces β in the ED-BIC case, but β remains remarkably high for the MD-BIC. The finite size also results in decay of the long-range interaction ($k_{\parallel}^{\text{res}} \neq 0$), which nevertheless persists over several micrometer distances for both BICs, offering significant enhancement relative to free space (see Supp. Info. Section C). While the ED-BIC presents a higher LDOS and CDOS, its β -factor is smaller. In what follows, we show that the β -factor is critical in determining entanglement generation over remote distances, which is made possible by BIC modes.

E. Concurrence

We now show that the metasurface enables the generation of long-range QE-QE entanglement. We quantify entanglement using the concurrence [39, 40]

$$C(t) = \max(0, \sqrt{\lambda_1} - \sqrt{\lambda_2} - \sqrt{\lambda_3} - \sqrt{\lambda_4}), \quad (4)$$

where λ_i are the eigenvalues, ordered by decreasing magnitude, of the non-Hermitian matrix $R = \rho\tilde{\rho}$, with $\tilde{\rho} = (\sigma_y \otimes \sigma_y)\rho^*(\sigma_y \otimes \sigma_y)$, in which conjugation is taken in the Pauli- Z basis. The concurrence satisfies $0 \leq C(t) \leq 1$ with the minimum 0 and maximum 1 occurring for separable and maximally entangled ρ , respectively.

We consider an initially uncorrelated state $|e_1g_2\rangle$ for the QEs in the electromagnetic vacuum. In this case, a closed expression of the concurrence can be found. To derive a useful approximate expression in terms of the β -factor, we further make the following assumptions: (i) the QEs interact solely via the BIC mode, such that $\Gamma_{12}(d)$ is given by Eq. (3); (ii) the QEs have the same LDOS, that is $\Gamma_{22} \simeq \Gamma_{11} = F_p\Gamma_0$; (iii) the regime is purely dissipative, that is, $\Omega_{12} \simeq 0$.

Fig. 4 shows that approximation (i) is valid for separations larger than a few lattice constant a , typically $d > 5a$ for the ED-BIC and $d > 2a$ for the MD-BIC (see also Supp. Info. Section E). Fig. 5 shows Γ_{22} and Ω_{12} as a function of d for both BIC types, along the same line-cuts as in Fig. 4. We see that approximation (ii) is valid at certain separations d and generally performs better for the ED-BIC, and that approximation (iii) typically performs well for $d > \lambda_0$.

Upon imposing approximations (i)-(iii), the concurrence becomes (Supp. Info. Section A)

$$C(t, d) \simeq \sinh(\bar{\beta}(d)F_p\Gamma_0 t) e^{-F_p\Gamma_0 t} \quad (5)$$

where $\bar{\beta}(d) \equiv \beta \text{osc}(d) \text{env}(d)$ is a d -dependent *effective* β -factor that accounts for finite-size effects and spectral mismatch. Figs. 6(a) and (b), show the evolution of the concurrence at $d = 5a = 2\mu\text{m}$, according to both the approximate expression in Eq. (5) (dashed grey curves),

and the exact expression in Eq. (4) (solid curves) evaluated by solving the two-QE master equation numerically using QuTIP [41, 42] (see Methods) with the parameters given in Table 1. Entanglement develops for both BIC types. Approximations (i)-(iii) are better satisfied for the ED-BIC [Fig. 6(a)], for which Eq. (5) therefore performs quantitatively better, though it captures the correct qualitative behaviour in both cases.

For large t , Eq. (5), converges to the population of the asymmetric Dicke state $\rho_{aa}(t)$ (see Supp. Info. Section B);

$$C(t, d) \simeq \frac{1}{2} e^{-(1-\bar{\beta}(d))F_p\Gamma_0 t} = \rho_{aa}(t). \quad (6)$$

A smaller F_p implies longer-lived entanglement, explaining why the concurrence decreases more slowly for the MD-BIC ($F_p \sim 14$) than for the ED-BIC ($F_p \sim 47$). It should be noted that the exponential decay of $C(t)$ is increasingly suppressed as $\bar{\beta}(d) \rightarrow 1$ in which case $C(t) \rightarrow 0.5$, yet the ED- and MD-BICs possess different $\bar{\beta}(d)$. For $d = 5a$ these are $\bar{\beta}(d) = 30.91\%$ and $\bar{\beta}(d) = 57.90\%$ respectively. For the ED-BIC, the maximum concurrence is smaller, occurs sooner, and decays faster, than for the MD-BIC. Solving $\partial C/\partial t = 0$ yields the time of maximum entanglement as

$$t_{\text{max}}(d) = \frac{1}{2F_p\Gamma_0\bar{\beta}(d)} \ln \left(\frac{1 + \bar{\beta}(d)}{1 - \bar{\beta}(d)} \right), \quad (7)$$

which yields the maximum concurrence

$$C_{\text{max}}(d) = \frac{\bar{\beta}(d)}{\sqrt{1 - \bar{\beta}(d)^2}} \left(\frac{1 + \bar{\beta}(d)}{1 - \bar{\beta}(d)} \right)^{-\frac{1}{2\bar{\beta}(d)}}. \quad (8)$$

This is a monotonically increasing function of $\bar{\beta}(d)$ alone, which is why it is larger in the case of the MD-BIC. On the other hand, t_{max} depends not only on $\bar{\beta}$, but is also proportional to $1/F_p$. Since F_p is larger for the ED-BIC, the maximum concurrence occurs sooner. We note, by way of contrast, that entanglement develops in free space 1 to 2 orders of magnitude later than for the ED-BIC and MD-BIC, and is significantly smaller in magnitude (see Supp. Info. Section F).

We plot $C_{\text{max}}(d)$ in Fig. 6, including both the numerical result computed using Eq. (4), and the approximation in Eq. (8) (dashed grey curves). The decaying envelope is expected for a finite metasurface, but entanglement nevertheless persists over distances exceeding several wavelengths, offering significant enhancement compared to free space and, for example, plasmonic slot waveguides [7, 19]. Analytic and numerical results agree reasonably well for $d \geq 5a$ in the ED-BIC case and $d \geq 2a$ in the MD-BIC case, and increasingly closer agreement can be expected as metasurface size increases.

III. CONCLUSIONS

We have shown that quasi-BICs in all-dielectric metasurfaces efficiently mediate long-range interactions be-

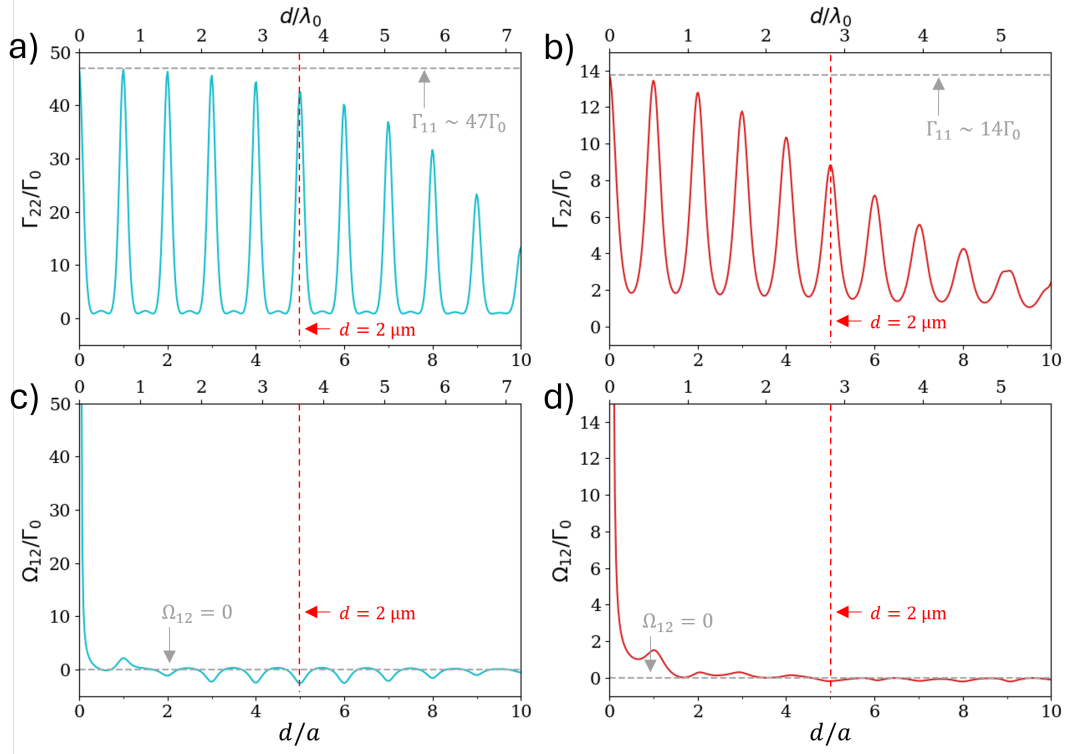


FIG. 5: (a) and (b): Decay rate Γ_{22} of the second quantum emitter as a function of emitter separation d for (a) the ED-BIC and (b) the MD-BIC. (c) and (d): Collective coupling rate Ω_{12} as a function of d for (c) the ED-BIC and (d) the MD-BIC. The rates are normalized by the free space single emitter decay rate Γ_0 .

	Γ_{11}/Γ_0	Γ_{22}/Γ_0	Γ_{12}/Γ_0	Ω_{12}/Γ_0
ED-BIC	46.9	42.4	15.3	-2.6
MD-BIC	13.7	8.8	7.9	-0.2

TABLE I: Parameters used in the numerical computation of the concurrence in Figs. 6 (a) and (b). The rates Γ_{11} are extracted from Figs. 2 (a) and (b) at $\lambda_0 = 552.0$ nm and $\lambda_0 = 708.9$ nm, respectively, and the rates Γ_{12} from Figs. 4 (a) and (b) at $d = 5a$ ($2\mu\text{m}$). The rates Γ_{22} and the rates Ω_{12} are extracted from Fig. 5 at $d = 5a$ ($2\mu\text{m}$).

tween QEs positioned 4 nm above the surface (near-field coupling). The ED-BIC and MD-BIC couple to out-of-plane and in-plane dipoles, respectively, and in the weak-coupling regime, their interactions with the QEs are governed entirely by the Purcell (F_P) and β -factors. For a finite metasurface, $F_P \sim 47$ and $\beta \sim 0.45$ for the ED-BIC, while the MD-BIC possesses a lower $F_P \sim 14$ and higher $\beta \sim 0.82$.

As a key application, we have computed the QE-QE entanglement generated when starting from the initial state $|e_1, g_2\rangle$ in the electromagnetic vacuum. The maximum concurrence C_{max} depends primarily on an effective $\bar{\beta}$ -factor that accounts for finite-size effects and QE-BIC frequency detuning. Since the MD-BIC possesses larger $\bar{\beta}$, it yields stronger entanglement, reaching $C_{\text{max}} \sim 0.25$ at a QE-QE separation of $2\mu\text{m}$, versus $C_{\text{max}} \sim 0.13$ for the ED-BIC. Entanglement is generated faster for the ED-BIC however, because the time of maximum entanglement is inversely proportional to F_P . We have shown

that at long times the concurrence decays exponentially with $F_P(1 - \bar{\beta})$, possessing ideal value $C_{\text{max}} = 0.5$ for $\bar{\beta} = 1$.

The separations we have considered span several wavelengths, $d \simeq 3.6\lambda_0$ for the ED-BIC and $d \simeq 2.8\lambda_0$ for the MD-BIC, but entanglement can persist at still larger distances. Increasing the metasurface size reduces finite-size effects, raising $\bar{\beta}$ and thus enhancing C_{max} . In the ideal limit of an infinite metasurface with perfect spectral matching, $\bar{\beta} \rightarrow \beta$ at all separations, enabling entanglement generation over arbitrary distances, provided $d \ll c/\Gamma_{11}$, beyond which the formalism breaks down [43]. Further optimization of metasurface design and materials could yield even higher β -factors. Their planar geometry and resulting integrability with 2D QE arrays, imply that metasurfaces are especially well-suited for realising scalable quantum technologies. While we have focused on two QEs, the formalism readily generalizes to many-body systems ($N > 2$) with interactions medi-

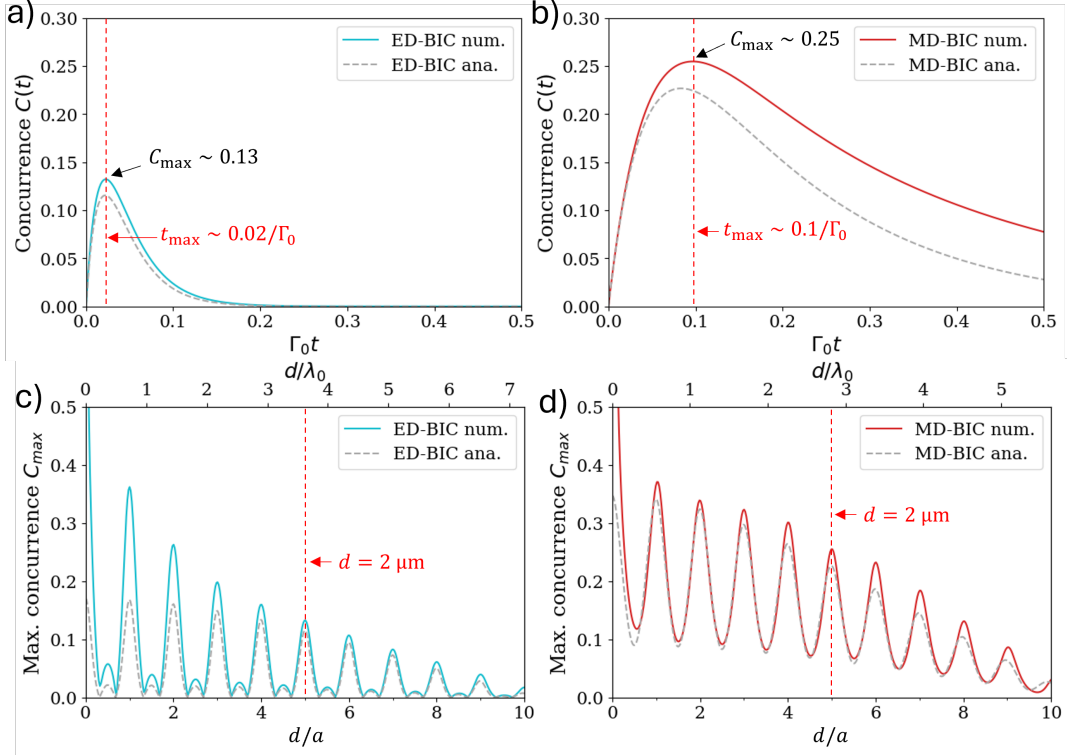


FIG. 6: Concurrence $C(t)$ with dimensionless time $\Gamma_0 t$ for a QE-QE separation of $d = 2 \mu\text{m}$ (5a) for the ED-BIC (a) and MD-BIC (b). Solid curves are found numerically (see Methods), while dashed grey curves are the results of Eq. (5), with $\bar{\beta} = 30.91\%$ for the ED-BIC and $\bar{\beta} = 57.90\%$ for the MD-BIC. The maximum ED-BIC concurrence $C_{\text{max}} = 0.13$ occurs at $t_{\text{max}} = 0.02/\Gamma_0$. The maximum MD-BIC concurrence $C_{\text{max}} = 0.25$ occurs at $t_{\text{max}} = 0.1/\Gamma_0$. The maximum concurrence $C_{\text{max}}(d)$ is plotted with d for the ED-BIC (c) and MD-BIC (d), with again, solid curves generated numerically (see Methods) and dashed grey curves generated from Eq. (8).

ated via the metasurface [44, 45]. Similarly, although for simplicity we have modeled the QEs as two-level systems, the extension to more realistic cases, including multi-level emitters and dephasing, is straightforward.

Methods

SMUTHI: We use the Python package SMUTHI [37] for the electromagnetic simulations of the coefficients Γ_{11} , Γ_{22} , Γ_{12} , and Ω_{12} . In all simulations, we make the electric and magnetic dipole approximations to model the metasurface, which involves setting the multipole order $l_{\text{max}} = 1$ in SMUTHI. This helps to speed-up simulations considerably, and is sufficiently accurate to capture the phenomena associated to the optical resonances of interest.

The LDOS Γ_{11}/Γ_0 is obtained by computing the left-hand-side of the relation $P/P_0 = \Gamma/\Gamma_0$. The power dissipated, P , and the corresponding free-space power P_0 , are calculated using SMUTHI.

The CDOS Γ_{12}/Γ_0 is obtained by expressing the dyadic Green's tensor in terms of the source electric field scattered by the metasurface, which is found using

SMUTHI. To construct the colourmap (Fig. 3), we sweep our observation point (the target dipole) over the entire metasurface, in the $z = R + h$ plane above the metasurface, to obtain the scattered electric field at each point, and from this, the associated collective decay rate.

CEMD: The coupled electric and magnetic dipole (CEMD) model developed in Refs. [34, 38] was used to calculate the collective decay rate for the infinite metasurface cases. For this purpose the self-consistent problem of the scattering of the electric source field of a dipole by an infinite metasurface is solved, where in the numerical implementation, the dipole source field is expanded in plane waves. The polarizabilities of the spherical particles are calculated using Mie theory.

QuTIP: We use the Quantum Toolbox In Python (QuTIP) [41, 42] to solve the master equation given in Supp. Info. Section B. The input master equation coefficients $\Gamma_{\mu\nu}$ and $\Omega_{\mu\nu}$ are the outputs of the SMUTHI computations. We assume a real transition dipole moment for both QEs with magnitude $p = 1 \times 10^{-29} \text{ Cm}$, which is roughly 3 Debye.

Acknowledgements

E.L. and R.P.-D. acknowledge initial discussions with Dmitry A. Kalashnikov that led to the formulation of this project. The authors would like to acknowledge the help of Daniel E. Eyles in performing the simula-

tions of the insets in Figures 2 (c)-(d) using SMUTHI. H.R. acknowledges the Turing scheme for supporting her stay in Singapore. E.L. and R.P.-D. acknowledge funding support from Singapore MTC-Programmatic Grant No. M21J9b0085.

IV. SUPPLEMENTARY INFORMATION FOR METASURFACE-MEDIATED QUANTUM ENTANGLEMENT VIA BOUND STATES IN THE CONTINUUM

A. Validity of the weak-coupling approximation

When an emitter is coupled to a nanophotonic environment, the condition for strong-coupling is usually given by [46]:

$$4g^2 > \frac{\Gamma_0^2 + \Gamma_{\text{BIC}}^2}{2} \quad (9)$$

where g is the coupling constant, Γ_0 is the emitter lifetime in free space and Γ_{BIC} is the lifetime of the mode to which the emitter couples to, which is a BIC mode in our case. The coupling constant g is related to the Purcell factor F_p as: $F_p = 4g^2/(\Gamma_0\Gamma_{\text{BIC}})$. The BIC lifetime is related to the linewidth or full width at half maximum (FWHM) as: $\Gamma_{\text{BIC}} \simeq 2\pi c \text{FWHM}/\lambda_{\text{BIC}}^2 = 2\pi c/(\lambda_{\text{BIC}}Q)$, where we defined the Q -factor of the BIC as: $Q = \lambda_{\text{BIC}}/\text{FWHM}$. Hence, the strong-coupling condition can be rewritten as:

$$F_p > \frac{\Gamma_0\lambda_{\text{BIC}}Q}{4\pi c} + \frac{\pi c}{\Gamma_0\lambda_{\text{BIC}}Q}. \quad (10)$$

The first term on the right hand side of the inequality is negligible compared to the second term, so the condition becomes:

$$F_p > \frac{\pi c}{\Gamma_0\lambda_{\text{BIC}}Q}. \quad (11)$$

In our case, for the ED-BIC, one has $F_p \sim 47$, $\lambda_{\text{BIC}} = 552 \text{ nm}$, $\text{FWHM} \sim 2 \text{ nm}$ and $Q \sim 276$ (see Fig. 2 in the main text). By using the expression of the emitter decay rate in free space: $\Gamma_0 = \omega_0^3 p^2 / (3\pi\epsilon_0\hbar c^3)$, the strong-coupling condition is met for dipole moments $p > p_{\text{max}} = 90 \cdot 10^{-29} \text{ Cm}$, which corresponds to approximately $p_{\text{max}} \sim 270$ debye. Similarly, for the MD-BIC, one has $F_p \sim 14$, $\lambda_{\text{BIC}} \sim 709 \text{ nm}$, $\text{FWHM} \sim 0.05 \text{ nm}$ and $Q \sim 14178$ (see Fig. 2 in the main text). The strong-coupling condition is thus met for dipole moments $p > p_{\text{max}} = 30 \cdot 10^{-29} \text{ Cm}$, which corresponds to approximately $p_{\text{max}} \sim 90$ debye. Therefore, the weak-coupling approximation made in this study will generally be valid for emitter dipole moment $p \ll 270$ debye in the ED-BIC case, and $p \ll 90$ debye in the MD-BIC case.

B. Quantum master equation formalism

We begin with the Hamiltonian describing two identical two-level dipoles ($\mu = 1, 2$) comprising an atomic (quantum emitter) system which is embedded within a dielectric medium,

$$\begin{aligned} H &= H_A + H_M + V \\ &= \sum_{\mu=1}^2 \frac{1}{2} \hbar \omega_0 \sigma_{\mu}^z + \int d^3\mathbf{r} \int_0^{\infty} d\omega \hbar \omega \mathbf{f}^{\dagger}(\mathbf{r}, \omega) \mathbf{f}(\mathbf{r}, \omega) + \sum_{\mu=1}^2 (\sigma_{\mu}^+ + \sigma_{\mu}^-) \mathbf{d} \cdot \mathbf{E}_M(\mathbf{R}_{\mu}). \end{aligned} \quad (12)$$

This Hamiltonian is given in the dipole gauge [36, 47] with the atomic part expressed in terms of the Pauli spin operators σ_{μ}^z and the transition frequency ω_0 , which corresponds to the transition from the ground to the excited state, $|g\rangle \rightarrow |e\rangle$. The medium Hamiltonian encompasses the total environment which is made up of the dielectric medium and free space. The operator-valued bosonic field variables $f_i(\mathbf{r}, \omega)$ and $f_i^{\dagger}(\mathbf{r}, \omega)$ represent the elementary excitations of the total environment. The interaction Hamiltonian V is decomposed in terms of Hermitian system and

environment operators. The electric field operators are defined in terms of the continuum of bosonic field operators and the respective dipole position \mathbf{R}_μ as

$$E_{M_j}^+(\mathbf{R}_\mu) = i\sqrt{\frac{\hbar}{\pi\epsilon_0}}\frac{1}{c^2}\int d^3\mathbf{r}'\int_0^\infty d\omega\omega^2\sqrt{\epsilon_I(\mathbf{r}',\omega)}G_{ji}(\mathbf{R}_\mu,\mathbf{r}',\omega)f_i(\mathbf{r}',\omega), \quad (13)$$

$$E_{M_j}^-(\mathbf{R}_\mu) = -i\sqrt{\frac{\hbar}{\pi\epsilon_0}}\frac{1}{c^2}\int d^3\mathbf{r}'\int_0^\infty d\omega\omega^2\sqrt{\epsilon_I(\mathbf{r}',\omega)}G_{ji}(\mathbf{R}_\mu,\mathbf{r}',\omega)f_i^\dagger(\mathbf{r}',\omega). \quad (14)$$

where $\epsilon_I(\mathbf{r},\omega) = 1 + \int_0^\infty d\tau\chi(\mathbf{r},t)e^{i\omega\tau}$ is the relative permittivity with dielectric susceptibility $\chi(\mathbf{r},t)$, and $G_{ij}(\mathbf{r},\mathbf{r}',\omega)$ is the dyadic Green's tensor. The dyadic Green's tensor governs the properties of the dielectric medium [48] and is key to bridging the gap between our quantum and classical nanophotonic formalisms. Note that there is an implicit summation over the cartesian coordinates i above and in the following.

We adopt a standard open systems approach to derive an equation of motion for the reduced density matrix of the two-emitter system [49]. After a lengthy but straightforward calculation, we arrive at the secular Born-Markov master equation,

$$\begin{aligned} \dot{\rho}_S(t) = & -i\sum_{\mu=\nu=1}^2 \tilde{\omega}_0[\sigma_\mu^+\sigma_\nu^-, \rho_S(t)] - i\sum_{\mu\neq\nu}^2 \Omega_{\mu\nu}[\sigma_\mu^+\sigma_\nu^-, \rho_S(t)] \\ & + \sum_{\mu,\nu=1}^2 \Gamma_{\mu\nu}(\omega_0) \left(\sigma_\mu^-\rho_S(t)\sigma_\nu^+ - \frac{1}{2}\{\sigma_\nu^+\sigma_\mu^-, \rho_S(t)\} \right), \end{aligned} \quad (15)$$

This equation is analogous to the master equation for two dipoles in free space [35, 50], with differences due to the presence of the dielectric medium contained within the coefficients.

Specifically, we have

$$\Omega_{\mu\nu}(\mathbf{R}_\mu, \mathbf{R}_\nu, \omega_0) = \frac{2\omega_0}{\hbar\pi\epsilon_0 c^2} P \int_0^\infty d\omega d_i d_j \Im(G_{ij}(\mathbf{R}_\mu, \mathbf{R}_\nu, \omega_0)) \frac{\omega^2}{\omega_0^2 - \omega^2}. \quad (16)$$

where the diagonal elements correspond to the (Lamb shift) self-energy interactions that modify the atomic transition frequencies,

$$\tilde{\omega}_0 = \omega_0 + \Omega_{\mu=\nu}, \quad (17)$$

and the off-diagonal elements correspond to the collective coupling rate

$$\Omega_{\mu\neq\nu} = -\frac{\omega_0^2}{\hbar\epsilon_0 c^2} d_i d_j \Re(G_{ij}(\mathbf{R}_\mu, \mathbf{R}_\nu, \omega_0)). \quad (18)$$

The total decay rate is defined as

$$\Gamma_{\mu\nu}(\mathbf{R}_\mu, \mathbf{R}_\nu, \omega_0) = \frac{2d_i d_j \omega_0^2}{\hbar\epsilon_0 c^2} \Im(G_{ij}(\mathbf{R}_\mu, \mathbf{R}_\nu, \omega_0)). \quad (19)$$

We have taken the zero temperature limit such that the bosonic occupation number $N = 0$.

The first term in equation Eq. (15) describes the coherent, unitary evolution of the system and is defined in the same way as in the single dipole case. The second term pertains to the off-diagonal dipole-dipole shifts with coherent collective coupling rate $\Omega_{\mu\neq\nu}$. These shifts contain spatial dependence arising from the Green's function and have no analogue in the single dipole case. In order to calculate $\Omega_{\mu\neq\nu}$, an integral over the entire spectrum must be performed. The integral can be evaluated through the introduction of an upper-frequency cut-off. Alternatively, using properties of the Green's function it is possible to simplify the calculation significantly. The full dyadic Green's function $G_{ij}(\mathbf{R}_\mu, \mathbf{R}_\nu, \omega)$ has no poles in the upper complex half-plane due to causality. This means that a Kramers-Kronig relation holds. When one takes the zero temperature limit ($N = 0$) of the dipole-dipole shift integral in Eq. (16), this relation may be used to yield the result in Eq. (18), which is given in terms of the real part of the full Green's function [51].

The final term in Eq. (15) describes dissipative emission processes with the associated rates $\Gamma_{\mu\nu}(\omega_0)$. Note that as we have taken the zero temperature limit, there are no absorption processes. The diagonal matrix elements yield the spontaneous (single-dipole) decay rates. The off-diagonal matrix elements correspond to the collective (inter-dipole) decay rates, which contain spatial dependence in the same way as the collective coupling rate. The decay

rates are given in terms of the imaginary part of the full Green's function as seen in Eq. (19). We remark that in deriving Eq. (15) we do not apply a rotating-wave approximation to the Hamiltonian, but instead perform a secular approximation to remove fast oscillating terms at the master equation level.

To solve the master equation we move from the computational basis to the collective Dicke basis $\{|e\rangle = |ee\rangle, |s\rangle = \frac{1}{\sqrt{2}}(|eg\rangle + |ge\rangle), |a\rangle = \frac{1}{\sqrt{2}}(|eg\rangle - |ge\rangle), |g\rangle = |gg\rangle\}$ as this best elicits the quantum nature of the interactions. The resulting differential equations for the Dicke basis atomic populations are given by

$$\dot{\rho}_{ee}(t) = -2\Gamma\rho_{ee}(t), \quad (20)$$

$$\dot{\rho}_{ss}(t) = -(\Gamma + \Gamma_{12})\rho_{ss}(t) - \frac{(\Gamma_{11} - \Gamma_{22})}{4}(\rho_{as}(t) + \rho_{sa}(t)) + (\Gamma + \Gamma_{12})\rho_{ee}(t), \quad (21)$$

$$\dot{\rho}_{aa}(t) = -(\Gamma - \Gamma_{12})\rho_{aa}(t) - \frac{(\Gamma_{11} - \Gamma_{22})}{4}(\rho_{as}(t) + \rho_{sa}(t)) + (\Gamma - \Gamma_{12})\rho_{ee}(t), \quad (22)$$

with the condition $\rho_{gg}(t) = 1 - \rho_{ee}(t) - \rho_{ss}(t) - \rho_{aa}(t)$, and for the relevant coherences we have

$$\dot{\rho}_{as}(t) = -(\Gamma - 2i\Omega_{12})\rho_{as}(t) - \frac{(\Gamma_{11} - \Gamma_{22})}{4}(\rho_{ss}(t) + \rho_{aa}(t) + 2\rho_{ee}(t)), \quad (23)$$

$$\dot{\rho}_{sa}(t) = -(\Gamma + 2i\Omega_{12})\rho_{sa}(t) - \frac{(\Gamma_{11} - \Gamma_{22})}{4}(\rho_{ss}(t) + \rho_{aa}(t) + 2\rho_{ee}(t)), \quad (24)$$

where $\Gamma = (\Gamma_{11} + \Gamma_{22})/2$ is the average of the two individual dipole decay rates and we have used $\Gamma_{12} = \Gamma_{21}$.

In general, the solutions to the above differential equations do not give much analytical insight, and so we solve them numerically for the corresponding plots given in the main text and elsewhere in this supporting information. However, in cases where $\Gamma_{11} = \Gamma_{22}$, as assumed for the approximate analytic concurrence expression given in the main text, the populations and coherences completely decouple. This leads to simplified differential equations

$$\dot{\rho}_{ee}(t) = -2\Gamma\rho_{ee}(t), \quad (25)$$

$$\dot{\rho}_{aa}(t) = -(\Gamma - \Gamma_{12})\rho_{aa}(t) + (\Gamma - \Gamma_{12})\rho_{ee}(t), \quad (26)$$

$$\dot{\rho}_{ss}(t) = -(\Gamma + \Gamma_{12})\rho_{ss}(t) + (\Gamma + \Gamma_{12})\rho_{ee}(t), \quad (27)$$

$$\dot{\rho}_{as}(t) = -(\Gamma - 2i\Omega_{12})\rho_{as}(t), \quad (28)$$

$$\dot{\rho}_{sa}(t) = -(\Gamma + 2i\Omega_{12})\rho_{sa}(t), \quad (29)$$

with the closed form analytical solutions

$$\rho_{ee}(t) = \rho_{ee}(0)e^{-2\Gamma t}, \quad (30)$$

$$\rho_{ss}(t) = \rho_{ss}(0)e^{-\Gamma_+ t} + \frac{\Gamma_+}{\Gamma_-}\rho_{ee}(0)(e^{-\Gamma_+ t} - e^{-2\Gamma t}), \quad (31)$$

$$\rho_{aa}(t) = \rho_{aa}(0)e^{-\Gamma_- t} + \frac{\Gamma_-}{\Gamma_+}\rho_{ee}(0)(e^{-\Gamma_- t} - e^{-2\Gamma t}), \quad (32)$$

$$\rho_{as}(t) = \rho_{as}(0)e^{-(\Gamma - 2i\Omega_{12})t}, \quad (33)$$

$$\rho_{sa}(t) = \rho_{sa}(0)e^{-(\Gamma + 2i\Omega_{12})t}. \quad (34)$$

Here we denote $\Gamma_+ = (\Gamma + \Gamma_{12})$ and $\Gamma_- = (\Gamma - \Gamma_{12})$, corresponding to decay rates enhanced (superradiant) and suppressed (subradiant) by collective effects, respectively. Such effects are characteristically quantum in nature. These modifications are present in free space for very small dipole separations, however they are significantly amplified by the presence of the dielectric medium. It should be noted that our solutions apply to the general case of two emitters in the presence of a medium, one need only to appropriately adjust the the Green's function ansatz and propagate it through.

1. Concurrence

In the case considered in the main text where initially only one quantum emitter is excited, the concurrence takes the analytical form [33]

$$C(t) = \sqrt{[\rho_{ss}(t) - \rho_{aa}(t)]^2 - [\rho_{sa}(t) - \rho_{as}(t)]^2}. \quad (35)$$

We see from Eq. (35) two limiting cases: (i) $t = 0$, for which the initial conditions correspond to $\rho_{ss}(0) = \rho_{aa}(0) = \rho_{as}(0) = 1/2$ and $\rho_{ee}(0) = 0$, and the concurrence is $C(0) = 0$, since the initial state is unentangled; and (ii) $t \rightarrow \infty$, where the concurrence is $C(\infty) \rightarrow 0$ since all excited populations and coherences decay exponentially in time (unless $\Gamma_{12} = \Gamma_{11}$, which is satisfied only for unseparated emitters or for a β -factor equal to unity, where $C(\infty) \rightarrow 0.5$). Therefore, entanglement is dynamically generated in the *transient* regime. By using the fact that $\rho_{sa}(t) = \rho_{as}^*(t)$, Eq. (35) can be rewritten as

$$C(t) = \sqrt{[\rho_{ss}(t) - \rho_{aa}(t)]^2 - 4[\text{Im}(\rho_{as}(t))]^2}. \quad (36)$$

Using the analytical expressions for the density matrix elements given above, we then find

$$C(t) = \frac{1}{2} \sqrt{[e^{-(\Gamma' + \Gamma_{12})t} - e^{-(\Gamma' - \Gamma_{12})t}]^2 + 4e^{-2\Gamma't} \sin^2(2\Omega_{12}t)}. \quad (37)$$

By making the approximations mentioned in the main text, $\Gamma_{22} \approx \Gamma_{11}$ and $\Omega_{12} \approx 0$, Eq. (37) simplifies to:

$$C(t) \simeq \sinh(\Gamma_{12}t) e^{-\Gamma_{11}t}. \quad (38)$$

This takes the form given in Eq. (6) of the main text once we approximate $\Gamma_{12} \approx \bar{\beta}(d)\Gamma_{11}$ and use the fact that $\Gamma_{11} = F_p\Gamma_0$.

C. Collective decay rate in free space

The collective decay rate and collective coupling rate in free space are given by Eqs. (1) and (2) in the main text, respectively, where \mathbf{G} is now the free space Green's function, given by [35]:

$$G_{ij}(\mathbf{R}_\mu, \mathbf{R}_\nu, \omega) = \frac{\omega}{4\pi c} (-\kappa_{ij}(\mathbf{R}_\mu, \mathbf{R}_\nu, \omega) \quad (39)$$

$$+ i\tau_{ij}(\mathbf{R}_\mu, \mathbf{R}_\nu, \omega)), \quad (40)$$

where

$$\begin{aligned} \kappa_{ij}(\mathbf{R}_\mu, \mathbf{R}_\nu, \omega) = & -(\delta_{ij} - \hat{R}_i \hat{R}_j) \frac{\cos(\theta)}{\theta} \\ & + (\delta_{ij} - 3\hat{R}_i \hat{R}_j) \left[\frac{\sin(\theta)}{\theta^2} + \frac{\cos(\theta)}{\theta^3} \right], \end{aligned} \quad (41)$$

and

$$\begin{aligned} \tau_{ij}(\mathbf{R}_\mu, \mathbf{R}_\nu, \omega) = & (\delta_{ij} - \hat{R}_i \hat{R}_j) \frac{\sin(\theta)}{\theta} \\ & + (\delta_{ij} - 3\hat{R}_i \hat{R}_j) \left[\frac{\cos(\theta)}{\theta^2} - \frac{\sin(\theta)}{\theta^3} \right], \end{aligned} \quad (42)$$

with $\theta = \frac{2\pi}{\lambda_0} \frac{R}{c}$, R is the magnitude of $\mathbf{R} = \mathbf{R}_\mu - \mathbf{R}_\nu$, and \hat{R}_i is the projection of the unit vector $\hat{\mathbf{R}} = \frac{\mathbf{R}}{R}$ along the i -axis ($i = x, y, z$). Note that the Green's tensor is symmetric under $\hat{\mathbf{R}} \rightarrow -\hat{\mathbf{R}}$. We plot the collective decay rate in free space in Fig. 7.

D. Derivation of the collective decay rate and β -factor [Eq. (3) in the main text]

1. Approximations over the Green function integral

The Green function of a system informs us about how the field propagates from one position to another in space. Once the Green function is known, the field scattered by a point dipole source located at \mathbf{r}_μ with dipole moment \mathbf{p} is given by

$$\mathbf{E}_s(\mathbf{r}) = \mathbf{G}(\mathbf{r}, \mathbf{r}_\mu) \mathbf{p}. \quad (43)$$

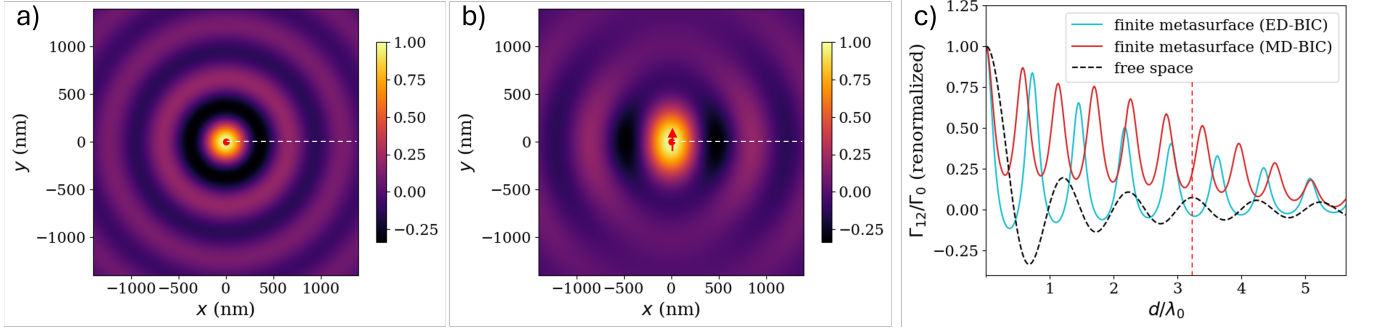


FIG. 7: a) and b) Collective decay rate Γ_{12} (normalized by Γ_0) in free space when the first emitter is located in the center (red dot) and the position of the second emitter is laterally scanned across the xy -plane. In a), both emitters have dipole moment along z -axis, and the wavelength is $\lambda_0 = 552.0$ nm (same configuration as in Fig. 3a in the main text without the metasurface). In b), both emitters have dipole moment along y -axis, and the wavelength is $\lambda_0 = 708.9$ nm (same configuration as in Fig. 3c in the main text without the metasurface). The areas correspond to the same areas shown in Fig. 3 in the main text for easier comparison. c) Collective decay rate Γ_{12} (normalized by Γ_0) in free space as a function of the emitters separation d (dashed black line), corresponding to cuts along the white dashed lines in a) and b), respectively (which are identical when the distance d is normalized by their respective wavelength λ_0). We also replotted the collective decay rates in the metasurface case from Fig. 4a-b in the main text (same color code), having renormalized them to their respective maximum (i.e. by the Purcell factor $F_p = 46.9$ and $F_p = 13.7$, respectively), and normalizing the distance d by $\lambda_0 = 552.0$ nm for ED-BIC and $\lambda_0 = 708.9$ nm for MD-BIC, for easier comparison with the free space case.

where \mathbf{r} is the observation point. In the framework of the coupled electric and magnetic dipole (CEMD) [38], the Green function of an *infinite* square periodic metasurface of lattice constant a can be expressed as an integral over the Brillouin zone:

$$\mathbf{G}(\mathbf{r}, \mathbf{r}_\mu) = \frac{a^2}{4\pi^2} \int_{\text{1BZ}} d\mathbf{k}_\parallel e^{i\mathbf{k}_\parallel(\mathbf{R}-\mathbf{R}_\mu)} \mathbf{G}_l(\mathbf{k}_\parallel, \boldsymbol{\rho}) [1/\boldsymbol{\alpha} - \mathbf{G}_b(\mathbf{k}_\parallel)]^{-1} \mathbf{G}_l(\mathbf{k}_\parallel, -\boldsymbol{\rho}_\mu), \quad (44)$$

where the dependence on the frequency ($k = \omega/c$) is understood. In this expression, $\mathbf{r} = \mathbf{R} + \boldsymbol{\rho}$ is the observational point and $\mathbf{r}_\mu = \mathbf{R}_\mu + \boldsymbol{\rho}_\mu$ the position of the dipole source, where the position is split in two components: \mathbf{R} is the lattice vector corresponding to the unit cell in which \mathbf{r} is located, while $\boldsymbol{\rho}$ is the position within the unit cell (and similar for \mathbf{R}_μ and $\boldsymbol{\rho}_\mu$) [20], while \mathbf{k}_\parallel is the perpendicular component of the wavevector, that is, $\mathbf{k}_\parallel = (k_x, k_y)$ (the metasurface is in the xy -plane). In addition, $\boldsymbol{\alpha}$ is the particle polarizability tensor, $\mathbf{G}_l(\mathbf{k}_\parallel, \mathbf{r})$ is the lattice Green function (how the field propagates from the metasurface at a given \mathbf{k}_\parallel) and $\mathbf{G}_b(\mathbf{k}_\parallel)$ is the depolarization Green function (how the lattice is depolarized) [38].

In general, the polarizability and the Green functions are matrices which expressions are relatively complicated. However, we know that, at the BIC frequency, the determinant of the renormalized polarizability $[1/\boldsymbol{\alpha} - \mathbf{G}_b(\mathbf{k}_\parallel)]$ has a real pole at $\mathbf{k}_\parallel = (0, 0)$. More specifically, the pole is at the zz component of the matrices (electric for MD-BIC and magnetic for ED-BIC), where the sub-index zz refers to the zz component of the matrices. Hence, we can consider that, close to the BIC frequency, the main contribution to the integral of Eq. (44) is given by the zz component of renormalized polarizability, $[1/\alpha_z - G_{b,zz}(\mathbf{k}_\parallel)]$, around $\mathbf{k}_\parallel \sim \mathbf{0}$. In the previous expression, α_z represents the electric or magnetic polarizability along the z -axis for MD-BIC and ED-BIC, respectively.

The ED-BIC state is characterized by an in-phase oscillation of electric dipoles along the z -axis. Therefore, at the ED-BIC frequency, the z component of the electric field scattered by the metasurface, $E_z^{\text{ED}}(\mathbf{r})$, when it is exited by a electric dipole placed at \mathbf{r}_μ and polarized along the z -axis with dipole moment p , can be approximated by the following integral

$$E_z^{\text{ED}}(\mathbf{r}) \simeq \frac{a^2}{4\pi^2} \int_{\text{1BZ}} d\mathbf{k}_\parallel e^{i\mathbf{k}_\parallel(\mathbf{R}-\mathbf{R}_\mu)} G_{l,zz}(\mathbf{k}_\parallel, \boldsymbol{\rho}) [1/\alpha_z - G_{b,zz}(\mathbf{k}_\parallel)]^{-1} G_{l,zz}(\mathbf{k}_\parallel, -\boldsymbol{\rho}_\mu) p, \quad (45)$$

Similarly, the MD-BIC state is characterized by an in-phase oscillation of magnetic dipoles along the z -axis. Thus, at the MD-BIC frequency, the y component of the electric field scattered by the metasurface, $E_y^{\text{MD}}(\mathbf{r})$, when it is exited by an electric dipole placed at \mathbf{r}_μ and polarized along the y -axis with dipole moment p can be approximated by

$$E_y^{\text{MD}}(\mathbf{r}) \simeq \frac{a^2}{4\pi^2} \int_{\text{1BZ}} d\mathbf{k}_\parallel e^{i\mathbf{k}_\parallel(\mathbf{R}-\mathbf{R}_\mu)} G_{l,yz}^{(EM)}(\mathbf{k}_\parallel, \boldsymbol{\rho}) [1/\alpha_z - G_{b,zz}(\mathbf{k}_\parallel)]^{-1} G_{l,yz}^{(EM)}(\mathbf{k}_\parallel, -\boldsymbol{\rho}_\mu) p, \quad (46)$$

where $G_{l,yz}^{(EM)}(\mathbf{k}_{\parallel}, \mathbf{r})$ is the component that relates the y component of the magnetic field produced by an electric dipole polarized along the z -axis, and vice-versa (z component of the electric field produced by an magnetic dipole polarized along the y -axis).

2. Green function expressions

For completeness, the zz component of the lattice Green functions are [38]:

$$\begin{aligned} G_{l,zz}(\mathbf{k}_{\parallel}, \mathbf{r}) &= \sum_{n,m=-\infty}^{\infty} G_{zz}(\mathbf{r}, \mathbf{r}_{nm}) e^{ik_x x} e^{ik_y y} \\ &= \sum_{l,p=-\infty}^{\infty} \frac{i}{2abk_z^{(l,p)}} \left[1 - \left(\frac{k_z^{(l,p)}}{k} \right)^2 \right] e^{i(k_x - \frac{2\pi}{a}l)x} e^{i(k_y - \frac{2\pi}{a}p)y} e^{ik_z^{(l,p)}|z|}, \end{aligned} \quad (47)$$

$$\begin{aligned} G_{l,yz}^{(EM)}(\mathbf{k}_{\parallel}, \mathbf{r}) &= \sum_{n,m=-\infty}^{\infty} G_{yz}^{(EM)}(\mathbf{r}, \mathbf{r}_{nm}) e^{ik_x x} e^{ik_y y} \\ &= \sum_{l,p=-\infty}^{\infty} \frac{i}{2a^2k_z^{(l,p)}} \left[-\frac{k_x - \frac{2\pi}{a}l}{k} \right] e^{i(k_x - \frac{2\pi}{a}l)x} e^{i(k_y - \frac{2\pi}{a}p)y} e^{ik_z^{(l,p)}|z|}, \end{aligned} \quad (48)$$

where $\mathbf{r}_{nm} = (na, ma)$ are the positions of the particles in the metasurface and $k_z^{(l,p)}$ is given by:

$$k_z^{(l,p)} = \sqrt{k^2 - \left(k_x - \frac{2\pi}{a}l\right)^2 - \left(k_y - \frac{2\pi}{a}p\right)^2}. \quad (49)$$

The zz component of the renormalized polarizability reads:

$$G_{b,zz}(\mathbf{k}_{\parallel}) = \lim_{\mathbf{r} \rightarrow \mathbf{0}} [G_{l,zz}(\mathbf{k}_{\parallel}, \mathbf{r}) - G_{zz}(\mathbf{r}, \mathbf{0})]. \quad (50)$$

In these expressions, $G_{zz}(\mathbf{r}, \mathbf{r}')$ is the zz component of the vacuum Green function:

$$G_{zz}(\mathbf{r}, \mathbf{r}') = \left(1 + \frac{\partial^2}{\partial z^2}\right) g(\mathbf{r}, \mathbf{r}'), \quad g(\mathbf{r}, \mathbf{r}') = \frac{e^{ik|\mathbf{r}-\mathbf{r}'|}}{4\pi|\mathbf{r}-\mathbf{r}'|}. \quad (51)$$

and $G_{yz}^{(EM)}(\mathbf{r}, \mathbf{r}')$ is the yz component of the vacuum Green function

$$G_{yz}^{(EM)}(\mathbf{r}, \mathbf{r}') = -\frac{\partial}{\partial x} g(\mathbf{r}, \mathbf{r}'). \quad (52)$$

3. Approximations over renormalized polarizability

Below diffraction, and in absence of absorption, the imaginary part of the renormalized polarizability appearing in Eqs. (45) and (46) reads:

$$\Im [1/\alpha_z - G_{b,zz}(\mathbf{k}_{\parallel})] = \frac{1}{2a^2k_z} \left(1 - \frac{k_z^2}{k^2}\right) \simeq \frac{1}{2a^2k} \frac{k_{\parallel}^2}{k^2}, \quad (53)$$

where k_z and k_{\parallel} defined as $k_z \equiv k_z^{(0,0)}$ and $k_{\parallel} \equiv |\mathbf{k}_{\parallel}|$, and in the last step, we take $k_z \sim k$, where this approximation is valid when $\mathbf{k}_{\parallel} \sim \mathbf{0}$.

On the other hand, the real part does not have a close-form expression, but around the BIC frequency and for $\mathbf{k}_{\parallel} \sim \mathbf{0}$, it can be approximated to

$$\Re [1/\alpha_z - G_{b,zz}(\mathbf{k}_{\parallel})] \simeq A(k_{BIC} - k) - B \frac{1}{2a^2k} \frac{k_{\parallel}^2}{k^2}, \quad (54)$$

where A and B are constants that depend on the specific case.

Thus, in our range of interest, the depolarization Green function can be approximated as follows:

$$[1/\alpha_z - G_{b,zz}(\mathbf{k}_{\parallel})]^{-1} = \frac{A(k_{BIC} - k) - B \frac{1}{2a^2k} \frac{k_{\parallel}^2}{k^2} + \frac{i}{2a^2k} \frac{k_{\parallel}^2}{k^2}}{\left[A(k_{BIC} - k) - B \frac{1}{2a^2k} \frac{k_{\parallel}^2}{k^2} \right]^2 + \left[\frac{1}{2a^2k} \frac{k_{\parallel}^2}{k^2} \right]^2}. \quad (55)$$

Therefore, close to the BIC frequency, the depolarization Green function exhibits a narrow resonance.

4. Approximations over the lattice Green function

The zz component of the lattice Green function appearing in Eq. (45) is:

$$\begin{aligned} G_{l,zz}(\mathbf{k}_{\parallel}, \mathbf{r}) &= e^{ik_x x} e^{ik_y y} \sum_{l,p=-\infty}^{\infty} \frac{i}{2abk_z^{(l,p)}} \left[1 - \left(\frac{k_z^{(l,p)}}{k} \right)^2 \right] e^{-i \frac{2\pi}{a} l x} e^{-i \frac{2\pi}{a} p y} e^{ik_z^{(l,p)} |z|}, \\ &= e^{ik_x x} e^{ik_y y} \tilde{G}_{l,zz}(\mathbf{k}_{\parallel}, \mathbf{r}), \\ &= e^{ik_x x} e^{ik_y y} \tilde{G}_{l,zz}(\mathbf{k}_{\parallel}, \boldsymbol{\rho}), \end{aligned} \quad (56)$$

where for convenience we factor out $e^{ik_x x} e^{ik_y y}$. In this way, $\tilde{G}_{l,zz}(\mathbf{k}_{\parallel}, \boldsymbol{\rho})$ is periodic, and for this reason we have changed \mathbf{r} by $\boldsymbol{\rho}$ in his evaluation.

Now, let us focus in the properties of $\tilde{G}_{l,zz}(\mathbf{k}_{\parallel}, \boldsymbol{\rho})$ and $\tilde{G}_{l,zz}(\mathbf{k}_{\parallel}, -\boldsymbol{\rho}_{\mu})$, specifically when $\boldsymbol{\rho} = (x, 0, z)$ and $\boldsymbol{\rho}_{\mu} = (0, 0, z)$, with z fixed and taking x as the variable (the source is fixed in space and the field is measured along the x -axis). First, at $\boldsymbol{\rho}_{\mu} = (0, 0, z)$, the lattice Green function reduce to

$$\tilde{G}_{l,zz}(\mathbf{k}_{\parallel}, (0, 0, z)) = \sum_{l,p=-\infty}^{\infty} \frac{i}{2abk_z^{(l,p)}} \left[1 - \left(\frac{k_z^{(l,p)}}{k} \right)^2 \right] e^{ik_z^{(l,p)} |z|}. \quad (57)$$

Since $k_z^{(l,p)}$ is purely imaginary $\forall (l, p)$ — except for $(l, p) = (0, 0)$ — below diffraction, the term $(l, p) = (0, 0)$ is a complex number, while the other are purely real

$$\tilde{G}_{l,zz}(\mathbf{k}_{\parallel}, (0, 0, z)) = \frac{i}{2abk_z} \frac{k_{\parallel}^2}{k^2} e^{ik_z |z|} + \sum_{l,p \neq 0} \frac{1}{2ab\tilde{k}_z^{(l,p)}} \left[1 + \left(\frac{\tilde{k}_z^{(l,p)}}{k} \right)^2 \right] e^{-\tilde{k}_z^{(l,p)} |z|}, \quad (58)$$

with $\tilde{k}_z^{(l,p)}$ defined as $\tilde{k}_z^{(l,p)} \equiv -ik_z^{(l,p)}$.

We can see that the complex term is proportional to k_{\parallel}^2 . Thus, at small k_{\parallel} (and for z not too far from the metasurface), the sum term will dominate (and the imaginary part would be much smaller than the real one).

a. N.B.: Notice that, due to the factor $e^{-\tilde{k}_z^{(l,p)} |z|}$, the dependence on z is exponential. Then, as we go further from the metasurface, the sum would eventually go to zero. This is why in Fig. 2c in the main text, the dependence of the total decay rate (the LDOS) of the first emitter located at position $\mathbf{r}_1 = (0, 0, z)$, which is proportional to $\Gamma_{11} \propto \Im[E_z^{\text{ED}}(\mathbf{r}_1)/p]$ and hence to $\Re[\tilde{G}_{l,zz}(\mathbf{k}_{\parallel}, \boldsymbol{\rho}_1) \tilde{G}_{l,zz}(\mathbf{k}_{\parallel}, -\boldsymbol{\rho}_1)]$, was well fitted by an exponential.

Also, considering that $\frac{2\pi}{a} > k > k_{\parallel}$, we can assume that $\tilde{k}_z^{(l,p)}$ does not depend on k nor on k_{\parallel} . With these assumptions, for small k_{\parallel} and moderate distance z , the lattice Green function can be approximated to a real function of z

$$\tilde{G}_{l,zz}(\mathbf{k}_{\parallel}, (0, 0, z)) \sim f(z). \quad (59)$$

with a small dependence on k and a negligible dependence on k_{\parallel} .

Now, let's see what is the dependence on x , by looking at $\boldsymbol{\rho} = (x, 0, z)$. In this case, the lattice Green function is

$$\tilde{G}_{l,zz}(\mathbf{k}_{\parallel}, (x, 0, z)) = \sum_{l,p=-\infty}^{\infty} \frac{i}{2abk_z^{(l,p)}} \left[1 + \left(\frac{k_z^{(l,p)}}{k} \right)^2 \right] e^{-i \frac{2\pi}{a} l x} e^{ik_z^{(l,p)} |z|}, \quad (60)$$

and, as before, below diffraction we have:

$$\tilde{G}_{l,zz}(\mathbf{k}_{\parallel}, \boldsymbol{\rho}) = \frac{i}{2abk_z} \frac{k_{\parallel}^2}{k^2} e^{ik_z|z|} + \sum_{l,p \neq 0} \frac{1}{2ab\tilde{k}_z^{(l,p)}} \left[1 + \left(\frac{\tilde{k}_z^{(l,p)}}{k} \right)^2 \right] e^{-i\frac{2\pi}{a}lx} e^{-\tilde{k}_z^{(l,p)}|z|}. \quad (61)$$

Again, the complex propagating term is proportional to k_{\parallel}^2 , so we will neglect it.

Due to that, at $\mathbf{k}_{\parallel} = (0, 0)$, $\tilde{k}_z^{(l,p)}$ is an even function, and as a first approximation we can say that it is also even for small k_{\parallel} . Thus, we get

$$\begin{aligned} \tilde{G}_{l,zz}(\mathbf{k}_{\parallel}, \boldsymbol{\rho}) &\simeq \sum_{l,p=1}^{\infty} \frac{2}{ab\tilde{k}_z^{(l,p)}} \left[1 + \left(\frac{\tilde{k}_z^{(l,p)}}{k} \right)^2 \right] \cos\left(\frac{2\pi}{a}lx\right) e^{-\tilde{k}_z^{(l,p)}|z|} \\ &+ \sum_{l=1}^{\infty} \frac{1}{ab\tilde{k}_z^{(l,0)}} \left[1 + \left(\frac{\tilde{k}_z^{(l,0)}}{k} \right)^2 \right] \cos\left(\frac{2\pi}{a}lx\right) e^{-\tilde{k}_z^{(l,0)}|z|} \\ &+ \sum_{p=1}^{\infty} \frac{1}{ab\tilde{k}_z^{(0,p)}} \left[1 + \left(\frac{\tilde{k}_z^{(0,p)}}{k} \right)^2 \right] e^{-\tilde{k}_z^{(0,p)}|z|}. \end{aligned} \quad (62)$$

where the propagating contribution is already neglected.

Similar to what we said before for the case $\boldsymbol{\rho}_{\mu} = (0, 0, z)$, assuming that $\tilde{k}_z^{(l,p)}$ mainly depend on l and p , we can express the lattice Green function as:

$$\tilde{G}_{l,zz}(\mathbf{k}_{\parallel}, \boldsymbol{\rho}) \simeq g(z, 0) + \sum_{l=1}^{\infty} (g_0(z, l) + 2g(z, l)) \cos\left(\frac{2\pi}{a}lx\right), \quad (63)$$

with

$$g(z, l) = \sum_{p=1}^{\infty} \frac{1}{ab\tilde{k}_z^{(l,p)}} \left[1 + \left(\frac{\tilde{k}_z^{(l,p)}}{k} \right)^2 \right] e^{-\tilde{k}_z^{(l,p)}|z|}, \quad (64)$$

$$g_0(z, l) = \frac{1}{ab\tilde{k}_z^{(l,0)}} \left[1 + \left(\frac{\tilde{k}_z^{(l,0)}}{k} \right)^2 \right] e^{-\tilde{k}_z^{(l,0)}|z|}, \quad (65)$$

where the prime in $\tilde{k}_z^{(l,p)}$ indicates that we take $\mathbf{k}_{\parallel} = (0, 0)$, i.e.,

$$\tilde{k}_z^{(l,p)} \sim \tilde{k}_z^{\prime(l,p)} \equiv \sqrt{\frac{4\pi^2}{a^2}(l^2 + p^2) - k^2}. \quad (66)$$

Then, the real function $g(z, l)$ (and $g_0(z, l)$) determines the contribution of each cosine to the sum.

Specifically, for the ED-BIC of silicon Mie-spheres of $n = 3.5$, and if we take $y = 0$ and $z = 104$ nm like the configuration in the main text, the cosine expansion of the field can be calculated as:

$$\tilde{G}_{l,zz}(\mathbf{k}_{\parallel}, (x, 0, z)) \propto 0.53 + \cos\left(\frac{2\pi}{a}x\right) + 0.31 \cos\left(\frac{4\pi}{a}x\right) + 0.0936 \cos\left(\frac{6\pi}{a}x\right) + 0.00258 \cos\left(\frac{8\pi}{a}x\right) + \dots \quad (67)$$

Following a similar derivation, for the MD-BIC case, it is possible to write the yz (electric-magnetic) component of the lattice Green function as

$$\begin{aligned} G_{l,yz}^{(EM)}(\mathbf{k}_{\parallel}, \mathbf{r}) &= e^{ik_x x} e^{ik_y y} \sum_{l,p=-\infty}^{\infty} \frac{i}{2abk_z^{(l,p)}} \left[-\frac{k_x - \frac{2\pi}{a}l}{k} \right] e^{ik_x - \frac{2\pi}{a}lx} e^{i - \frac{2\pi}{a}py} e^{ik_z^{(l,p)}|z|}, \\ &= e^{ik_x x} e^{ik_y y} \tilde{G}_{l,yz}^{(EM)}(\mathbf{k}_{\parallel}, \boldsymbol{\rho}), \end{aligned} \quad (68)$$

Below diffraction, we have

$$\tilde{G}_{l,yz}^{(EM)}(\mathbf{k}_{\parallel}, \boldsymbol{\rho}) = -\frac{i}{2abk_z} \frac{k_x}{k} e^{ik_z|z|} + \sum_{l,p \neq 0} \frac{1}{2ab\tilde{k}_z^{(l,p)}} \left[-\frac{k_x - \frac{2\pi}{a}l}{k} \right] e^{-i\frac{2\pi}{a}lx} e^{-i\frac{2\pi}{a}py} e^{-\tilde{k}_z^{(l,p)}|z|}, \quad (69)$$

and assuming that at $\mathbf{k}_{\parallel} = (0, 0)$, $\tilde{k}_z^{(l,p)}$ is an even function, as a first approximation we can say that

$$\begin{aligned} \tilde{G}_{l,yz}^{(EM)}(\mathbf{k}_{\parallel}, \boldsymbol{\rho}) \approx & -\frac{i}{2abk_z} \frac{k_x}{k} e^{ik_z|z|} + 2i \sum_{l,p \neq 0} \frac{1}{ab\tilde{k}_z^{(l,p)}} \left[-\frac{2\pi}{a}l \right] \sin\left(\frac{2\pi}{a}lx\right) \cos\left(\frac{2\pi}{a}py\right) e^{-\tilde{k}_z^{(l,p)}|z|} \\ & - 2 \sum_{l,p \neq 0} \frac{1}{ab\tilde{k}_z^{(l,p)}} \left[-\frac{k_x}{k} \right] \cos\left(\frac{2\pi}{a}lx\right) \cos\left(\frac{2\pi}{a}py\right) e^{-\tilde{k}_z^{(l,p)}|z|}, \end{aligned} \quad (70)$$

and further assuming that k_x is small

$$\tilde{G}_{l,yz}^{(EM)}(\mathbf{k}_{\parallel}, \boldsymbol{\rho}) \approx 2i \sum_{l,p \neq 0} \frac{1}{ab\tilde{k}_z^{(l,p)}} \left[-\frac{2\pi}{a}l \right] \sin\left(\frac{2\pi}{a}lx\right) \cos\left(\frac{2\pi}{a}py\right) e^{-\tilde{k}_z^{(l,p)}|z|}. \quad (71)$$

Specifically, for the MD-BIC of silicon Mie-spheres of $n = 3.5$, and if we take $\boldsymbol{\rho} = (x, y, z)$ with $x = 0.164a$ and $z = 104$ nm like the configuration in the main text, the cosine expansion of the field can be calculated as:

$$\tilde{G}_{l,yz}^{(EM)}(\mathbf{k}_{\parallel}, (0.164a, y, z)) \propto 1 + 0.547 \cos\left(\frac{2\pi}{a}y\right) + 0.0088 \cos\left(\frac{4\pi}{a}y\right) + 0.00014 \cos\left(\frac{6\pi}{a}y\right) + \dots \quad (72)$$

Note that in both cases, in first order, the lattice Green functions do not depend on \mathbf{k}_{\parallel} .

5. Cross density of states integral

In base of the previous approximations, the cross density of states (CDOS) associated to the ED-BIC is proportional to $\Gamma_{12} \propto \Im[E_z^{\text{ED}}(\mathbf{r})/p]$ (the metasurface is excited by an electric dipole along the z axis),

$$\Im[E_z^{\text{ED}}(\mathbf{r})/p] \simeq \frac{a^2}{4\pi^2} \int_{\text{1BZ}} d\mathbf{k}_{\parallel} \Im \left\{ e^{ik_x x} [1/\alpha_z - G_{b,zz}(\mathbf{k}_{\parallel})]^{-1} \right\} \Re \left[\tilde{G}_{l,zz}(\mathbf{k}_{\parallel}, \boldsymbol{\rho}) \tilde{G}_{l,zz}(\mathbf{k}_{\parallel}, -\boldsymbol{\rho}_{\mu}) \right] \quad (73)$$

where we have already neglected the imaginary part of $\tilde{G}_{l,zz}(\mathbf{k}_{\parallel}, \boldsymbol{\rho})$.

Since the depolarization Green function represents a narrow resonance around $\mathbf{k}_{\parallel} \sim \mathbf{0}$, and the lattice Green functions do not depend on \mathbf{k}_{\parallel} at small \mathbf{k}_{\parallel} , we can separate them as

$$\Im[E_z^{\text{ED}}(\mathbf{r})/\mu] \simeq \frac{a^2}{4\pi^2} \Re \left[\tilde{G}_{l,zz}(\mathbf{k}_{\parallel}, \boldsymbol{\rho}) \tilde{G}_{l,zz}(\mathbf{k}_{\parallel}, -\boldsymbol{\rho}_{\mu}) \right] \int_{\text{1BZ}} d\mathbf{k}_{\parallel} \Im \left\{ e^{ik_x x} [1/\alpha_z - G_{b,zz}(\mathbf{k}_{\parallel})]^{-1} \right\}. \quad (74)$$

and with the help of the next integrals

$$\int_0^{2\pi} \cos(k_{\parallel}(\cos \theta x + \sin \theta y)) d\theta = 2\pi J_0\left(k_{\parallel} \sqrt{x^2 + y^2}\right), \quad (75)$$

$$\int_0^{2\pi} \sin(k_{\parallel}(\cos \theta x + \sin \theta y)) d\theta = 0, \quad (76)$$

to show that

$$\begin{aligned} \Gamma_{12}(x) & \propto \Re \left[\tilde{G}_{l,zz}(\mathbf{k}_{\parallel}^{\text{res}}, \boldsymbol{\rho}) \tilde{G}_{l,zz}(\mathbf{k}_{\parallel}^{\text{res}}, -\boldsymbol{\rho}_{\mu}) \right] \times J_0(k_{\parallel}^{\text{res}}|x|) \\ & \sim \left[\sum \gamma_j \cos\left(j \frac{2\pi}{a}x\right) \right] \times J_0(k_{\parallel}^{\text{res}}|x|), \end{aligned} \quad (77)$$

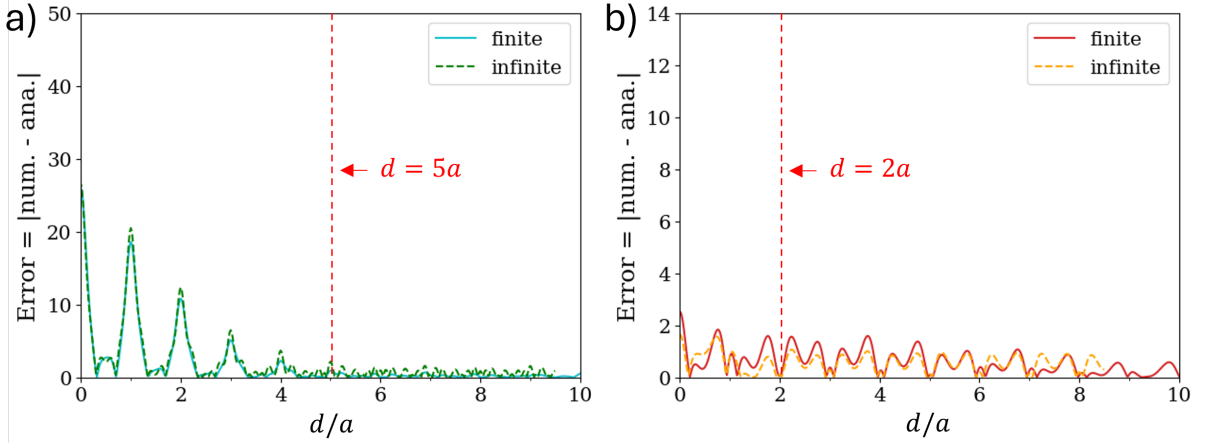


FIG. 8: Absolute error between numerics and analytics for the collective decay rate, in the case of (a) the ED-BIC and (b) the MD-BIC.

where $\mathbf{k}_{\parallel}^{\text{res}}$ is the \mathbf{k}_{\parallel} at which the depolarization Green function resonates and $k_{\parallel}^{\text{res}} \equiv |\mathbf{k}_{\parallel}^{\text{res}}|$ (closer to zero as the frequency is closer to the BIC frequency), and the coefficients γ_j , when particularized for the ED-BIC of silicon Mie-spheres, are the ones from Eq. (67).

Similarly, the CDOS associated to the MD-BIC is proportional to $\Gamma_{12} \propto \Im[E_y^{\text{MD}}(\mathbf{r})/p]$ (the metasurface is exited by an electric dipole along the y axis), and with a similar procedure as for the ED-BIC, we get

$$\begin{aligned} \Gamma_{12}(y) &\propto \Re \left[\tilde{G}_{l,yz}^{(EM)}(\mathbf{k}_{\parallel}^{\text{res}}, \boldsymbol{\rho}) \tilde{G}_{l,yz}^{(EM)}(\mathbf{k}_{\parallel}^{\text{res}}, -\boldsymbol{\rho}_{\mu}) \right] \times J_0(k_{\parallel}^{\text{res}}|y|) \\ &\sim \left[\sum \gamma_j \cos \left(j \frac{2\pi}{a} y \right) \right] \times J_0(k_{\parallel}^{\text{res}}|y|), \end{aligned} \quad (78)$$

where the coefficients γ_j , when particularized for the MD-BIC of silicon Mie-spheres, are the ones from Eq. (72).

6. β -factor

The most important figure-of-merit in this paper is the β -factor. Similar to photonic crystal waveguides [30–32], we define here the single-emitter β -factor associated to the BIC mode, which gives the probability of the photon to be emitted into the BIC mode, as:

$$\beta = \frac{\Gamma_{\text{BIC}}}{\Gamma} \quad (79)$$

where Γ is the total single-emitter decay rate, and Γ_{BIC} is the decay rate into the BIC mode.

Γ_{BIC} is in fact given by Eqs. (77) and (78) when $x = 0$ and $y = 0$ for the ED- and MD-BIC, respectively, since the CDOS corresponds to the LDOS for 0 separations. Hence, for the ED-BIC (and similarly for the MD-BIC), $\Gamma_{\text{BIC}} = \Gamma_{12}(x = 0)$, which according to Eq. (77) gives:

$$\Gamma_{\text{BIC}} = C \sum \gamma_j \quad (80)$$

with C a pre-factor (undetermined). Then, we express C in terms of the β -factor using Eq. (80) in Eq. (79) as:

$$C = \frac{\Gamma \beta}{\sum \gamma_j} \quad (81)$$

Hence, Eq. (3) in the main text is obtained from Eqs. (77) and (78) and by replacing the pre-factor C by the above expression in terms of the β -factor and the total single-emitter decay rate (where the denominator of C is used to renormalized the coefficients of the cosine expansion).

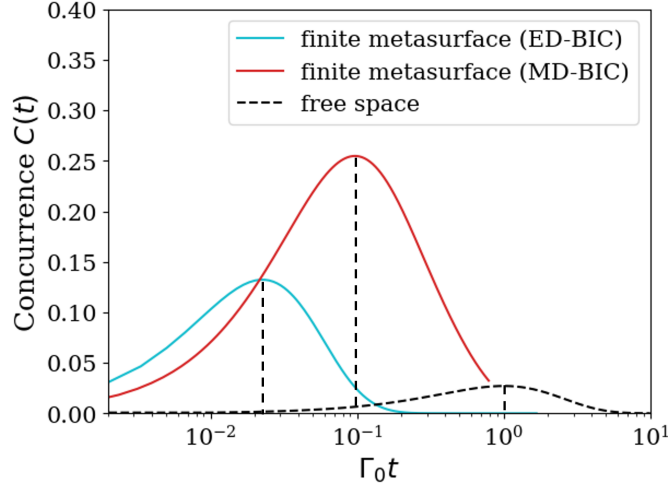


FIG. 9: Concurrence in free space as a function of the normalized time $\Gamma_0 t$ (dashed black line) calculated for emitters separation which is near $d \sim 2 \mu\text{m}$ ($d = 1.79 \mu\text{m}$ if $\lambda_0 = 552.0 \text{ nm}$ or $d = 2.30 \mu\text{m}$ if $\lambda_0 = 708.9 \text{ nm}$). For comparison, we also replotted the concurrences in the metasurface case from Fig. 6(a) and (b) in the main text (same color code). The vertical dashed lines occur at the time where the concurrence reaches its maximum. Note that the horizontal axis is now in log scale.

E. Collective decay rate: error between numerics and analytics

In Fig. 8 we plot the absolute error between the numerical and analytical collective decay rates for both the ED-BIC and the MD-BIC.

F. Concurrence in free space

In free space, $\Gamma_{11} = \Gamma_{22} = \Gamma_0$, and since we consider an emitters separation which corresponds to the fourth maximum of Γ_{12} (highlighted by red vertical dashed line in Fig. 7c), where $\Gamma_{12} = 0.0736 \Gamma_0$ and $\Omega_{12} = 0$, Eq. (38) above is exact [52]. We plot this concurrence given by Eq. (38) as a function of time in Fig. 9.

-
- [1] P. Lodahl, S. Mahmoodian, and S. Stobbe, *Rev. Mod. Phys.* **87**, 347 (2015), URL <https://link.aps.org/doi/10.1103/RevModPhys.87.347>.
 - [2] J. B. Trebbia, Q. Deplano, P. Tamarat, and B. Lounis, *Nature Commun.* **13**, 2962 (2022), 2109.10584.
 - [3] I. Aharonovich, J.-P. Tetienne, and M. Toth, *Nano Letters* **22**, 9227 (2022), pMID: 36413674, <https://doi.org/10.1021/acs.nanolett.2c03743>, URL <https://doi.org/10.1021/acs.nanolett.2c03743>.
 - [4] L. Zundel, A. Cuartero-González, S. Sanders, A. I. Fernández-Domínguez, and A. Manjavacas, *ACS Photonics* **9**, 540 (2022), <https://doi.org/10.1021/acsphotonics.1c01463>, URL <https://doi.org/10.1021/acsphotonics.1c01463>.
 - [5] C. M. Holland, Y. Lu, and L. W. Cheuk, *Science* **382**, 1143 (2023), <https://www.science.org/doi/pdf/10.1126/science.adf4272>, URL <https://www.science.org/doi/abs/10.1126/science.adf4272>.
 - [6] F. Shah, T. L. Patti, O. Rubies-Bigorda, and S. F. Yelin, *Phys. Rev. A* **109**, 012613 (2024), 2306.08555.
 - [7] A. Gonzalez-Tudela, D. Martin-Cano, E. Moreno, L. Martin-Moreno, C. Tejedor, and F. J. Garcia-Vidal, *Physical review letters* **106**, 020501 (2011).
 - [8] A. Asenjo-Garcia, M. Moreno-Cardoner, A. Albrecht, H. J. Kimble, and D. E. Chang, *Phys. Rev. X* **7**, 031024 (2017), URL <https://link.aps.org/doi/10.1103/PhysRevX.7.031024>.
 - [9] A. Albrecht, L. Henriot, A. Asenjo-Garcia, P. B. Dieterle, O. Painter, and D. E. Chang, *New Journal of Physics* **21**, 025003 (2019), URL <https://dx.doi.org/10.1088/1367-2630/ab0134>.
 - [10] A. S. Sheremet, M. I. Petrov, I. V. Iorsh, A. V. Poshakinskiy, and A. N. Poddubny, *Reviews of Modern Physics* **95**, 015002 (2023).
 - [11] A. Tiranov, V. Angelopoulou, C. J. van Diepen, B. Schriniski, O. A. D. Sandberg, Y. Wang, L. Midolo, S. Scholz, A. D. Wieck, A. Ludwig, et al., *Science* **379**, 389 (2023), <https://www.science.org/doi/pdf/10.1126/science.ade9324>, URL <https://www.science.org/doi/abs/10.1126/science.ade9324>.
 - [12] W. Ji, J. Chang, H.-X. Xu, J. R. Gao, S. Gröblacher, H. P. Urbach, and A. J. L. Adam, *Light Sci Appl* **12**, 169 (2023).

- [13] Z. Zheng, D. Rocco, H. Ren, O. Sergaeva, Y. Zhang, K. B. Whaley, C. Ying, D. de Ceglia, C. De-Angelis, M. Rahmani, et al., *Nanophotonics* **12**, 4255 (2023), URL <https://doi.org/10.1515/nanoph-2023-0526>.
- [14] A. V. Kildishev, A. Boltasseva, and V. M. Shalaev, *Science* **339**, 1232009 (2013), <https://www.science.org/doi/pdf/10.1126/science.1232009>, URL <https://www.science.org/doi/abs/10.1126/science.1232009>.
- [15] N. Yu and F. Capasso, *Nature materials* **13** **2**, 139 (2014), URL <https://api.semanticscholar.org/CorpusID:25771706>.
- [16] C. Soukoulis and M. Wegener, *Nature Photonics* **5**, 523 (2011).
- [17] G. W. Castellanos, P. Bai, and J. Gómez Rivas, *Journal of Applied Physics* **125**, 213105 (2019), ISSN 0021-8979, https://pubs.aip.org/aip/jap/article-pdf/doi/10.1063/1.5094122/13318709/213105_1_online.pdf, URL <https://doi.org/10.1063/1.5094122>.
- [18] *Nat. Photon.* **17** (2023).
- [19] P. K. Jha, N. Shitrit, J. Kim, X. Ren, Y. Wang, and X. Zhang, *ACS Photonics* (2017), URL <https://api.semanticscholar.org/CorpusID:46764505>.
- [20] L. Zundel, A. Cuartero-González, S. Sanders, A. I. Fernández-Domínguez, and A. Manjavacas, *ACS Photonics* **9**, 540 (2022).
- [21] C. W. Hsu, B. Zhen, A. Stone, J. Joannopoulos, and M. Soljačić, *Nature Reviews Materials* **1**, 16048 (2016).
- [22] S. Neale and E. A. Muljarov, *Phys. Rev. B* **103**, 155112 (2021), URL <https://link.aps.org/doi/10.1103/PhysRevB.103.155112>.
- [23] K. L. Koshelev, Z. F. Sadrieva, A. A. Shcherbakov, Y. S. Kivshar, and A. A. Bogdanov, *Phys. Usp.* **66**, 494 (2023), URL <https://ufn.ru/en/articles/2023/5/c/>.
- [24] J. von Neuman and E. Wigner, *Physikalische Zeitschrift* **30**, 467 (1929).
- [25] L. Fonda and R. G. Newton, *Annals of Physics* **10**, 490 (1960), ISSN 0003-4916, URL <https://www.sciencedirect.com/science/article/pii/0003491660901196>.
- [26] S. T. Ha, Y. H. Fu, N. K. Emani, Z. Pan, R. M. Bakker, R. Paniagua-Domínguez, and A. I. Kuznetsov, *Nature nanotechnology* **13**, 1042 (2018).
- [27] M. Wu, S. T. Ha, S. Shendre, E. G. Durmusoglu, W.-K. Koh, D. R. Abujetas, J. A. Sánchez-Gil, R. Paniagua-Domínguez, H. V. Demir, and A. I. Kuznetsov, *Nano Letters* **20**, 6005 (2020).
- [28] M. Wu, L. Ding, R. P. Sabatini, L. K. Sagar, G. Bappi, R. Paniagua-Domínguez, E. H. Sargent, and A. I. Kuznetsov, *Nano letters* **21**, 9754 (2021).
- [29] A. Canaguier-Durand and R. Carminati, *Physical Review A* **93**, 033836 (2016).
- [30] G. Lecamp, P. Lalanne, and J. Hugonin, *Physical review letters* **99**, 023902 (2007).
- [31] V. Manga Rao and S. Hughes, *Physical Review B—Condensed Matter and Materials Physics* **75**, 205437 (2007).
- [32] M. Arcari, I. Söllner, A. Javadi, S. Lindskov Hansen, S. Mahmoodian, J. Liu, H. Thyrrstrup, E. H. Lee, J. D. Song, S. Stobbe, et al., *Physical review letters* **113**, 093603 (2014).
- [33] R. Tanaś and Z. Ficek, *Journal of Optics B: Quantum and Semiclassical Optics* **6**, S90 (2004).
- [34] D. R. Abujetas and J. A. Sánchez-Gil, *Nanomaterials* **11** (2021), ISSN 2079-4991, URL <https://www.mdpi.com/2079-4991/11/4/998>.
- [35] G. S. Agarwal, *Quantum Optics* (Cambridge University Press, 2012).
- [36] A. Stokes and A. Nazir, *New Journal of Physics* **20**, 043022 (2018).
- [37] A. Egel, K. M. Czajkowski, D. Theobald, K. Ladutenko, A. S. Kuznetsov, and L. Pattelli, *Journal of Quantitative Spectroscopy and Radiative Transfer* **273**, 107846 (2021).
- [38] D. R. Abujetas, J. Olmos-Trigo, J. J. Sáenz, and J. A. Sánchez-Gil, *Phys. Rev. B* **102**, 125411 (2020), URL <https://link.aps.org/doi/10.1103/PhysRevB.102.125411>.
- [39] W. K. Wootters, *Phys. Rev. Lett.* **80**, 2245 (1998), URL <https://link.aps.org/doi/10.1103/PhysRevLett.80.2245>.
- [40] W. Wootters, *Quantum Information & Computation* **1**, 27 (2001).
- [41] J. Johansson, P. Nation, and F. Nori, *Computer Physics Communications* **183**, 1760 (2012), URL <https://www.sciencedirect.com/science/article/pii/S0010465512000835>.
- [42] N. Lambert, E. Giguère, P. Menczel, B. Li, P. Hopf, G. Suárez, M. Gali, J. Lishman, R. Gadhvi, R. Agarwal, et al., *Qutip 5: The quantum toolbox in python*, arXiv:2412.04705, URL <https://arxiv.org/abs/2412.04705>.
- [43] J. Kästel and M. Fleischhauer, *Physical Review A—Atomic, Molecular, and Optical Physics* **71**, 011804 (2005).
- [44] Alvarez-Giron and P. Barberis-Blostein, *J. Phys. A: Math. Theor.* **53** (2020).
- [45] S. Ribeiro and S. A. Gardiner, *Phys. Rev. A* **105**, L021701 (2022), URL <https://link.aps.org/doi/10.1103/PhysRevA.105.L021701>.
- [46] P. Törmä and W. L. Barnes, *Reports on Progress in Physics* **78**, 013901 (2014).
- [47] A. Stokes and A. Nazir, *Rev. Mod. Phys.* **94**, 045003 (2022), URL <https://link.aps.org/doi/10.1103/RevModPhys.94.045003>.
- [48] L. Knoll, S. Scheel, and D.-G. Welsch, *Qed in dispersing and absorbing media* (2003), quant-ph/0006121.
- [49] H.-P. Breuer and F. Petruccione, *The Theory of Open Quantum Systems* (Oxford University Press, 2007), ISBN 9780199213900, URL <https://doi.org/10.1093/acprof:oso/9780199213900.001.0001>.
- [50] A. Stokes and A. Nazir, *New Journal of Physics* **20**, 043022 (2018), URL <https://dx.doi.org/10.1088/1367-2630/aab29d>.
- [51] D. Dzotjan, J. Kästel, and M. Fleischhauer, *Phys. Rev. B* **84**, 075419 (2011), URL [10.1103/PhysRevB.84.075419](https://doi.org/10.1103/PhysRevB.84.075419).
- [52] Indeed, in free space Γ_{12} and Ω_{12} are in quadrature, i.e. $\pi/2$ out-of-phase, see Eqs. (41) and (42).